# Flow Models for a Vortex Cell

R. Donelli* and P. Iannelli*
*Centro Italiano Ricerche Aerospaziali, 81043 Capua, Italy*
S. Chernyshenko[†]
*Imperial College London, London, England SW7 2AZ, United Kingdom*
A. Iollo[‡]
*Université Bordeaux 1 33405 Talence, France*
and
L. Zannetti[§]
*Politecnico di Torino, 10129 Torino, Italy*

**The flow inside a vortex trapping cavity is simulated by a suite of models: point vortex, Prandtl–Batchelor flow, and Reynolds-averaged Navier–Stokes equations. The scope is to ascertain to what extent an inviscid model can be used to design vortex cells. It turns out that the Prandtl–Batchelor flow, with an appropriate jump in the Bernoulli constant across the dividing streamline, gives an acceptable representation of the solution found by the Reynolds-averaged Navier–Stokes equations, which in turn compares well with experimental results when an appropriate turbulence model is selected.**

## Nomenclature

| | | |
|---|---|---|
| $a_n, b_n$ | = | coefficients of the Theodorsen–Garrick transform |
| $C_f$ | = | skin-friction coefficient |
| $c_p$ | = | pressure coefficient |
| $H(\cdot)$ | = | Heaviside function |
| $h$ | = | characteristic length |
| $L$ | = | cavity opening |
| $M$ | = | strength of a doublet on physical $z$ plane |
| $p$ | = | pressure |
| $q_\infty$ | = | physical velocity at infinity |
| $s$ | = | curvilinear coordinate along the cavity wall |
| $U_e$ | = | velocity at the boundary-layer edge |
| $\mathbf{U}$ | = | velocity vector in the physical plane |
| $w$ | = | complex potential |
| $x, y$ | = | physical coordinates |
| $x_v, y_v$ | = | vortex physical coordinates |
| $z$ | = | complex variable of the physical complex plane |
| $\beta$ | = | jump in the Bernoulli constant |
| $\gamma$ | = | trapped vortex circulation |
| $\delta(\cdot)$ | = | Dirac function |
| $\delta$ | = | boundary-layer thickness |
| $\delta_L$ | = | laminar sublayer thickness |
| $\epsilon$ | = | internal angle at $A$ |
| $\zeta, \lambda, \nu$ | = | complex variable of auxiliary plane |
| $\vartheta_A$ | = | argument of point $A$ on the $\sigma$ plane |
| $\mu$ | = | complex variable of the unit circle plane |
| $\mu_\infty$ | = | image of the point at infinity of the physical plane |
| $\mu_v$ | = | trapped vortex location |
| $\mu = \mu_A$ | = | trailing-edge image |
| $\bar{\mu}_v$ | = | $1/\mu_v^\star$ |
| $\nu_V$ | = | complex variable of the auxiliary plane corresponding to the vortex |
| $\nu_A$ | = | complex variable of the auxiliary plane corresponding to point $A$ |
| $\nu_B$ | = | complex variable of the auxiliary plane corresponding to point $B$ |
| $\rho$ | = | density |
| $\sigma$ | = | complex variable of the hodograph plane |
| $\sigma_b$ | = | centroid of the regular curve obtained on the $\sigma$ plane |
| $\Gamma_d, \Gamma_u, \Gamma_l, \Gamma_r$ | = | lower, upper, left, and right boundaries of $\Omega$ |
| $\varphi_\infty$ | = | $\arg(\mu_\infty)$ |
| $\psi$ | = | stream function |
| $\psi_0$ | = | auxiliary function |
| $\psi'$ | = | preliminary Green's function |
| $\Omega$ | = | rectangular subset of a plane |
| $\omega$ | = | $\nabla \times \mathbf{U}$ |

*Applied Aerodynamics Laboratory.
†Department of Aeronautics, Prince Consort Road.
‡Institut de Mathématiques de Bordeaux Unité Mixte de Recherche 5251 and Institut National de Recherche en Informatique et en Automatique équipe-pro.
§Dipartimento di Ingegneria Aeronautica e Spaziale.

## I.   Introduction

SEPARATED flows past bluff bodies are usually unsteady. A vortex formed by separation is shed downstream, then a new vortex is formed, and the process repeats itself periodically or chaotically. This results in a wake consisting of large intensive vortices of significant kinetic energy. A body moving through a fluid and generating such a wake has to experience large drag. This way of explaining the high drag in separated flows emphasizes the fact that the large magnitude of the drag is caused by unsteady large-scale vortex shedding rather than by the separation itself. If the separation eddy were not shed downstream but remained in the vicinity of the body, then the wake generation would require less energy, and the drag would be reduced. Such a steady separation eddy is called a trapped vortex.

In spite of the long history of research and the general attractiveness of the idea, trapped vortices are not used in practice for lifting surfaces. In recent decades, however, progress has been made in understanding flows of this type and in the technology of active flow control. As a result, one can see a clear path of research and development which should lead to practical solutions using trapped vortices. This paper represents one step along this path.

So far, there have been only two reportedly successful implementations of this idea, namely, the Kasper wing [1] and the EKIP (Ecology and Progress) aircraft [2].[¶] Kasper [1] observed a high-lift condition while flying his glider. Kasper hypothesized that the high lift was due to a trapped vortex above the wing. EKIP aircraft was designed, built, and flight-tested in Russia at the end of 1980s through the early 1990s. EKIP fully utilized the idea of a vortex cell (discussed in more detail to follow) thus representing a more advanced concept. We refer to both of these implementations as only reportedly successful because extensive wind-tunnel tests of a model of the Kasper wing, reported by Kruppa [3], confirmed neither the high-lift coefficient observation nor the proposed vortex structure, and because we are not aware of any publications in peer-reviewed journals confirming or at least documenting the efficiency of EKIP. One of the authors (S. Chernyshenko) attended seminar presentations at the Moscow University, where the EKIP designer, Professor L. N. Schukin, claimed that the fuel efficiency of the flight-tested radio-controlled EKIP models (the largest had a wingspan of about 2 m, cited from memory) was comparable to that of a small conventional aircraft, while our colleague, Professor G. Yu. Stepanov, visited the Saratov Aviation Plant and inspected the largest of the flying models and also the unfinished larger aircraft. Note also that certain features of the available sketches of EKIP aircraft are in remarkable agreement with qualitative conclusions obtained and published independently, as discussed next. Note also that Wu and Wu [4] gave a plausible explanation, also discussed later, of the reason for the discrepancy between wind-tunnel tests and flight experiments on the Kasper wing. Therefore, both the Kasper wing and EKIP deserve at least the benefit of a doubt, but, overall, the viability of the trapped vortex concept is yet to be confirmed. It crucially depends on the issue of vortex stability, and it can therefore be favorably affected by advances in active flow control techniques.

Before considering the stability, several notes on the application of the point-vortex or Föppl model to separated flows in general and to flows with trapped vortices in particular should be made. In that model, the (necessarily two-dimensional) flow is assumed to be potential and having singular points, so that all the vorticity inside the eddy is concentrated inside a point vortex. Probably, the very first use of the Föppl model in the context of trapped vortices was made by Ringleb [5]. Unfortunately, Ringleb erroneously ignored the so-called Routh rule [6], and some of his results were incorrect [7]. Nevertheless, Ringleb's contribution is noted for the role it played in the dissemination of the idea of a trapped vortex [5].

For certain body shapes, steady Föppl flow satisfying the Kutta condition does not exist. This led to series of studies (see, for example, Rossow [8]) aimed at modifying the body shape or introducing additional singularities (sinks) to ensure the existence of the steady solution. Such a modification can be and sometimes is called vortex stabilization because, if a steady solution does not exist, the flow has to remain unsteady. However, for the full Navier–Stokes equations, the existence of a steady two-dimensional solution is proved mathematically [9] (strictly speaking, it is done for flows in closed domains, but this does not seriously affect our argument, because the domain can be arbitrary large). Therefore, the problem of nonexistence of steady solutions within the Föppl model is an artifact of the imperfection of that model and does not reflect any real physics of the flow.

Another problem of the point-vortex model is related to the nonuniqueness of the flow. Typically, one can arbitrarily prescribe the circulation of the vortex and then find the corresponding flow. If the body has a sharp edge, the circulation is often chosen in such a way as to satisfy the Kutta–Joukowski condition on the edge. Unfortunately, this is completely unphysical. In fact, real flows always have a mixing layer along the dividing streamline that is the streamline separating the closed-streamline eddy and the external flow. The inviscid flow modeling the real one should have a tangential discontinuity that is a jump in the Bernoulli constant across the dividing streamline. This jump is another arbitrary

parameter, in addition to the amount of vorticity in the eddy. Detailed analysis shows that it is the Bernoulli constant jump which is determined by the Kutta condition, rather than the amount of vorticity inside the eddy. The point-vortex model postulates, however, a zero Bernoulli constant jump across the dividing streamline; hence, using the Kutta condition for determining vortex circulation should be done with great caution, if at all. This understanding was mostly achieved in the course of research on high-Reynolds-number asymptotics of steady separated flows. The main ideas relevant to the issue at hand were formulated in the famous paper by Batchelor [10], whereas a comprehensive analysis directly applicable to (assumed laminar) flows with trapped vortices is given in [11] (see the latter paper for references to the substantial body of work done in between). The corresponding analysis is complicated mathematically, but the main physical idea is simple. Consider the flow shown in Fig. 1, which also illustrates the idea of a vortex cell discussed later. The flow separates at the cusp and reattaches somewhere downstream. The fluid in the eddy rotates clockwise. Friction at the wall slows down the rotation, whereas friction in the mixing layer accelerates it. The rotation speed adjusts itself so that these two effects are in balance. One can imagine that the dividing streamline is replaced with a moving lid; then, the Kutta condition becomes irrelevant while the physics of the balance remains the same.

Interestingly, in the cases when the suction flow rate was nonzero, the work of Rossow [8] gives a rare example of the case when using the Kutta condition to determine the point-vortex circulation is appropriate. In this work, suction is supposed to be applied through the side walls bounding the area with a trapped vortex. In the two-dimensional point-vortex approximation, this suction is modeled with a sink, the position of which coincides with the position of the vortex. Then, the flow has no area of closed streamlines, and the Batchelor's analysis does not apply. However, because the pressure drop between the incoming flow and the point vortex is infinite, the power required to implement the suction is also infinite in this case. In reality, this power will be finite, but too large for the approach to be practical.

In spite of the shortcomings, the point-vortex model can be used for investigating flows with trapped vortices, but both the decision on the applicability of this model to a particular problem and the interpretation of the results do require deep understanding of much wider and more complex issues of fluid dynamics than the point-vortex model itself.

Steady solutions of the Navier–Stokes equations are usually unstable. In the high-Reynolds-number flows encountered in practice, this is always the case; moreover, even the boundary layers upstream of the separation would often be turbulent. The flow stabilization in a rigorous sense would therefore require full control of turbulence, which is a very difficult task indeed. Fortunately, as Wu and Wu [4] pointed out, for achieving a significant drag reduction, one needs to prevent only the large-scale vortex shedding
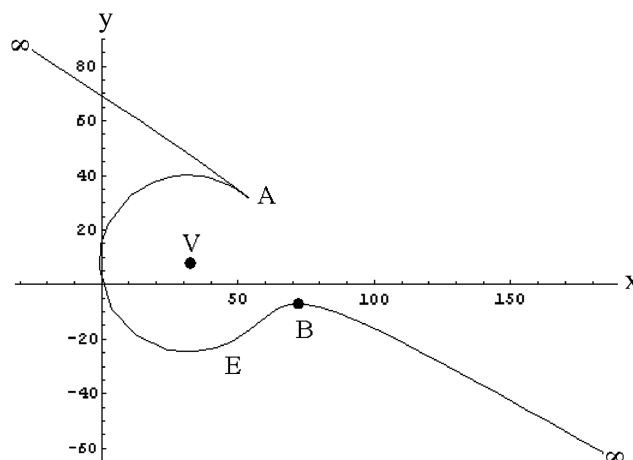
**Fig. 1   Physical $z$ plane.**

rather than to fully suppress turbulence. We will here consider vortex stabilization in this sense. Stabilization can be achieved by various means. First of all, there are geometries for which, while the flow is separated, large-scale vortex shedding does not occur (see [12] or the experimental parts of [13,14]). In these cases, however, the dividing streamline could be replaced with a solid wall on which the pressure gradient would be favorable, so that the flow would not be separated anyway, and the vortex cell is not actually needed. Stabilization can be achieved by constant suction inside the eddy, as in the EKIP aircraft [2] or in the experiments of Riddle et al. [15]. In EKIP, this suction was combined with vortex cells having central bodies inside. Suction is, however, an active form of control in the sense that it requires energy. Therefore, it makes sense to consider more complicated forms of control in the hope of reducing energy consumption. One step up in complexity would be an open-loop control, say, by imposing some oscillations on the flow. In particular, Wu and Wu [4] suggested that wing vibrations led to stabilization of the trapped vortex in the Kasper flight tests, thus explaining the discrepancy with the wind-tunnel tests. This motivated a study using the Föppl model [16] which demonstrated that superposition of oscillations can indeed stabilize the flow with a trapped vortex. In a related but somewhat wider than flow with trapped vortices context, open-loop and closed control is extensively reviewed in Cattafesta et al. [17]. In principle, closed-loop control should be most efficient, and its effectiveness in the application to separated flows past bluff bodies was experimentally demonstrated in the recent paper by Pastoor et al. [18], in which an extensive literature review is also given. These latest results leave little doubt about the feasibility of stabilization of large-scale vortex shedding by flow control, even though there is yet a ways to go in terms of commercial viability of such systems.

Suppose now that the vortex stabilization technology is available. Then, what is the sensible geometry of the airfoil with a trapped vortex? In short, the answer is that the trapped vortex should be accommodated in a vortex cell that is a specially designed cavity in the airfoil surface. The theoretical foundations of this requirement emerged in the studies of high-Reynolds-number asymptotics of steady separated flows (see [11,19] and further references therein). Although the mathematics involved is complicated, the physics of this requirement is quite simple. It turns out that, for almost any shape of the airfoil/cavity, the flow in the recirculating eddy separates again, creating another region of closed streamlines. Such secondary separation results in a flow of a more complicated topology and with more inflections points in the velocity profiles, which should therefore be more difficult to stabilize. Also, even if it is stabilized, such a flow would have large velocity gradients and, hence, a higher rate of energy dissipation leading to higher drag. Judging by the available sketches [2] and photographs[¶], EKIP designers could arrive at a similar conclusion about the benefits of carefully designing the vortex cell shape.

Within the framework of steady (stabilized) flow, the effect of a trapped vortex can be usefully interpreted in terms of a comparison of two airfoils: the actual airfoil with a vortex cavity and an airfoil obtained by replacing the dividing streamline with a solid wall. Suppose that the shape of this second airfoil is such that the flow past it exhibits massive separation with the separation point somewhere on the segment of the wall replacing the dividing streamline. Then, the flow past the airfoil with the cavity and outside the vortex can be interpreted as a flow past the second airfoil but with a section of the wall moving with the velocity of the flow on the dividing streamline. One can now say that the vortex cell prevents massive separation by the same mechanism as a moving wall. It may seem natural that this "moving wall" should be placed where the separation would occur otherwise. However, it can also make sense to position the vortex cell further upstream. Its effect will then consist of making the velocity profile in the boundary layer more filled, thus postponing the separation. These two mechanisms can, of course, be combined. As far as a secondary separation inside the cell is concerned, it may seem that it should be possible to find such a shape of the cell that pressure will only grow in the flow direction along the dividing streamline and then decrease along the cell wall, thus eliminating the possibility of a

secondary separation inside the cell. However, rigorous results [11] suggest that the presence of a section of a wall inside the cell with an unfavorable pressure gradient is inevitable: a vortex cell cannot eliminate unfavorable pressure gradient; rather, it redistributes it over the wall inside the cell (see [20,21] for further references and discussions concerning the ways an unfavorable gradient can be eliminated). This is the major reason why the cavity shape should be carefully designed rather than selected by trial and error.

It should now be obvious that successful practical implementation of the idea of a trapped vortex requires progress in several areas. These include vortex stabilization techniques, turbulence modeling applicable to stabilized (that is, without large-scale vortex shedding but still turbulent) flow, and vortex cell shape optimization methods. Turbulence modeling presents a significant problem, because so far there are only limited experimental data on turbulent separated flows with trapped vortices. Note that turbulence models tuned to separated flows with large-scale vortex shedding do not apply to flows with trapped vortices. At the same time, because shape optimization is involved, fast methods for calculating the trapped vortex flow are needed. It was suggested in [11] that these two problems can be resolved by adjusting the laminar high-Reynolds-number theory of flows with trapped vortices to simulation of real flows. In that theory, viscosity manifests itself in a most pronounced way in thin boundary and mixing layers. It was proposed that the model for simulating a turbulent flow with a trapped vortex can be obtained from the high-Reynolds-number asymptotic theory by replacing the laminar viscosity in the boundary and mixing layers with turbulent viscosity. This is advantageous because then turbulence needs to be modeled in a thin layer and this is easier, and because numerical calculations within such a model are fast.

The inviscid component of the high-$Re$ asymptotic model is the Batchelor-model flow [10]. With the position of the separation point fixed at the vortex cell cusp, there is a one-parameter family of Batchelor-model flows for a given cell geometry. The value of this parameter is determined by the processes in the thin viscous layers. Hence, the validity of the methods of determining this parameter (Bernoulli constant jump in the following sections) in the case of a turbulent flow needs to be investigated. To this end, a special experimental facility was built [22] and encouraging results were obtained; however, this work is still in progress and it is far beyond the scope of the present paper. Another issue of applying this approach to turbulent flow is that, strictly speaking, the Prandtl–Batchelor theorem [23] does not apply to turbulent flows. Therefore, even if the value of the parameter of the Batchelor-model flow is correctly found, the possibility of approximating the turbulent flow with the Batchelor model needs to be verified. This is the main goal of the present paper. First, using a simple point-vortex approach, we design a vortex cell shape which can be expected to be representative of the future, more properly designed, vortex cells. We also develop a numerical approach for calculating inviscid flows with trapped vortices. Then, we calculate the flow in that vortex cell using Reynolds-averaged Navier–Stokes (RANS) equations with turbulence models selected on the basis of the data available in the literature. We then calculate the same flow using the Batchelor model, adjust its parameter to fit the RANS solution, and compare the flow patterns and the pressure and velocity fields.

## II.   Design of the Vortex Cavity

In this section, we detail the model and the assumptions employed to design the vortex cavity. The vortex cavity has been designed according to a variation of the classical Kirchhoff hodograph-plane method (see, for instance, [24]). The same approach as the present one has been used in [21].

Briefly, the method solves the inverse problem of finding the shape of a wall, with a trapping vortex cavity, that realizes a prescribed velocity distribution. To explain the method and to illustrate the kind of wall we are looking for, we first describe a typical solution. Figure 1 shows an example of wall geometry as obtained by the inverse method. The wall extends to infinity, the flow is characterized by an asymptotic uniform velocity $q_\infty$ flowing from the left-hand

side. The flow detaches at the sharp cusp $A$ and reattaches at $B$. A dividing streamline connecting $A$ to $B$, not depicted in the figure, separates the external flow from the flow entrained by a vortex inside the cavity. The flow is assumed as irrotational; the vortex is thus a point singularity located in $V$.

The design velocity is such that there are no adverse pressure gradients on the solid wall. In fact, following the external flow past the wall, the flow accelerates from the upstream infinity to the edge $A$; along the nonsolid separatrix, the flow decelerates from $A$ to $B$, where it reaches a stagnation point, then accelerates from $B$ to the downstream infinity. Inside the cavity, the flow accelerates from the stagnation point $B$ to a point $E$, and then holds a constant velocity from $E$ to the cusp $A$. The pressure equilibrium at $A$ requires that the value of such constant velocity has to be the same as the external flow separating at $A$.

To describe the hodograph-plane method, let us define the physical plane of the motion as the complex $z$ plane, with $z = x + iy$. Because the flow is assumed as irrotational, a complex potential $w = \varphi + i\psi = w(z)$ and a complex velocity $(dw)/(dz) = u - iv = \sigma(z)$ will exist, with $\varphi$, $\psi$, and $u$, $v$ being the velocity potential, the stream function, and the Cartesian velocity components, respectively.

Let the hodograph plane be defined as the complex $\sigma$ plane, with $\sigma = u - iv$. The design velocity distribution to be realized along the wall forms a figure on the hodograph plane. This is the starting datum selected by the designer. Basically, the problem is solved by exploiting the knowledge of this datum to find the analytical relationship $\sigma = f(w)$ between the complex velocity $\sigma = dw/dz$ and the complex potential $w(z)$. Once such a relationship is found, the problem is solved by way of the Kirchhoff method by integrating the differential equation $dz/dw = 1/f(w)$ along the streamline $\psi = \psi_0$ which corresponds to the wall, that is,

$$z_0 = \int_{-\infty}^{+\infty} [1/f(\varphi + i\psi_0)]\,d\varphi$$

The small variation of our approach takes advantage of using an auxiliary $\nu$ plane and finding the relationships $\sigma = g(\nu)$ and $w = w(\nu)$. The problem is then solved by integrating the differential equation $dz/d\nu = (dw/d\nu)/g(\nu)$, that is, $z = \int [(dw/d\nu)/g(\nu)]_{\nu_0}\,d\nu$.

To describe the details of the design method, let us consider Fig. 2, where the initial datum on the hodograph plane that yields the wall of Fig. 1 is shown. Let us describe the wall velocity contour by starting from the upstream infinity and following the solid wall contour. In the hodograph plane, we follow the velocity contour in clockwise direction starting from the point labeled $\infty$.

From $\infty$ to the cusp $A$, the complex velocity accelerates along an arc of a circle which goes through the origin. Inside the cavity, we

follow the contour in a direction opposite to the flow. The complex velocity holds a constant value between $A$ and $E$, its contour is thus an arc of a circle centered on the origin. From $E$ to $B$, the velocity contour follows a circular arc, with $B$, which corresponds to a stagnation point, located into the origin. Outside the cavity, the flow then expands downstream from $B$ to the asymptotic velocity at infinity $\infty$.

The velocity at $A$ has been assumed as the reference velocity, and the points $E$, $B$, $\infty$, and $A$ are assumed to belong to the same circle. Such scheme defines a single infinity family of contours, with the argument $\vartheta_A$ of the complex velocity in $A$ ($\vartheta_A = \arg(dw/dz)_A$) being a free parameter. The choice of this parameter defines cavities with larger or smaller openings.

In general, the present method is capable of solving the inverse problem for any arbitrary velocity contour with proper regularity conditions. The choice of a velocity profile formed by two circular arcs has been made to solve the problem in closed analytical form. In fact, the method is based on conformal mapping and circular arcs can be easily managed by elementary functions.

On the hodograph plane, the entire velocity field past the wall is represented by the domain external to the design contour. The point at infinity $\sigma = \infty$ corresponds to the vortex located in the point $z_V$ of the physical $z$ plane. The method of solution is based on conformally mapping this domain onto the imaginary-positive half-plane of the auxiliary complex $\nu$ plane shown in Fig. 3.

Let $\sigma = g(\nu)$ denote the $\nu \to \sigma$ mapping function:

$$\sigma = \frac{dw}{dz} = g(\nu)$$

and let $\epsilon$ denote the internal angle at $A$; it is

$$\epsilon = \frac{\pi}{2} - \vartheta_A$$

where $\vartheta_A$ is the argument of point $A$ on the $\sigma$ plane. Taking $\tau = 2 - \epsilon/\pi$, the transformation

$$\left(\frac{\sigma - \sigma_A}{\sigma + \bar{\sigma}_A}\right)^{1/\tau} = \frac{a\nu + b}{c\nu + 1} \tag{1}$$

maps the exterior of the figure of the $\sigma$ plane onto the upper half-plane of the $\nu$ plane. This is accomplished by a proper selection of the $a$, $b$, and $c$ complex parameters. In fact, according to the Riemann mapping theorem, the transformation is unique once the correspondence between three points or, equivalently, six real conditions are established.

By expressing explicitly $\nu$ as $\nu = \nu(\sigma)$, the coefficients $a$, $b$, and $c$ are defined by the following conditions:

$$|g(\infty) - g(\sigma_C)| = R \quad \text{Im}[\nu(\sigma_B)] = 0 \quad \nu(\sigma_B) = -\nu(\sigma_A) \quad \nu(\infty) = i$$

where $\sigma_C$ and $R$ denote the center and the radius of the $EBC$ arc of the contour on the $\sigma$ plane. These conditions establish that the $\sigma$ contour is mapped on the real axis of the $\nu$ plane, that the detachment and reattachment ($A$, $B$) points are symmetrically located with respect to the origin, and that the point corresponding to the vortex $\sigma_V = \infty$ is mapped onto the imaginary axis at $\nu_V = i$. It has to be noted that the actual location of the point $\infty$ on the $\sigma$ contour is a result of the mapping definition and cannot be defined a priori. However, it can be
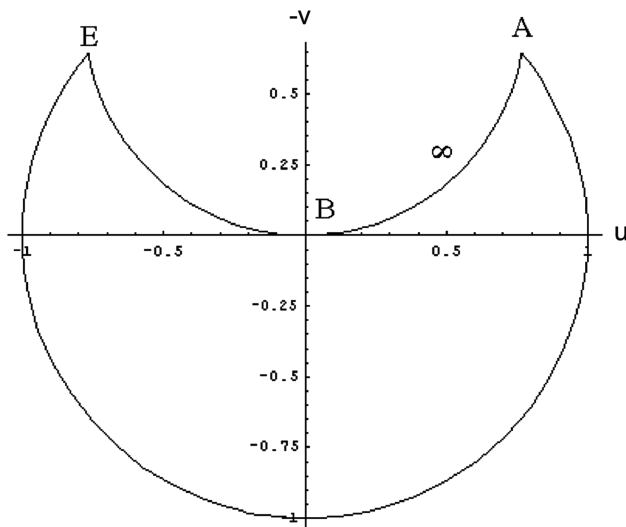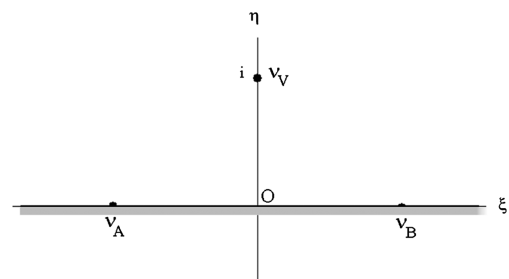
Fig. 2  Hodograph $\sigma$ plane.

Fig. 3  Auxiliary $\nu$ plane ($\nu = \xi + i\eta$).

shown that the preceding conditions assure that the point $\infty$ belongs to the arc $BA$.

According to the Riemann mapping theorem, we can state that there exists a unique $z = z(\nu)$ mapping, so far unknown, that maps the $\nu$-plane domain onto the $z$-plane physical domain, and such that $\nu_A \to z_A$, $\nu_B \to z_B$, and $\nu_V \to z_V$. The complex potential of the motion, which is invariant under conformal mapping, can be thus be defined as

$$w = Q_\infty \nu + \frac{\gamma}{2\pi i} \log\left(\frac{\nu - i}{\nu + i}\right)$$

which is pertinent to an asymptotic uniform flow with a vortex located in $\nu_\nu = i$ and with the real axis as a streamline.

The complex velocity on the $\nu$ plane results in

$$\frac{dw}{d\nu} = Q_\infty + \frac{\gamma}{2\pi i}\left(\frac{1}{\nu - i} - \frac{1}{\nu + i}\right)$$

The Kutta condition

$$\left(\frac{dw}{d\nu}\right)_{\nu_A} = 0$$

defines the vortex circulation $\gamma$:

$$\gamma = -\pi Q_\infty(\nu_A^2 + 1)$$

The complex potential, as defined, is pertinent to a flow which has the asymptotic velocity $Q_\infty$, detaches at $\nu_A$, and, for the symmetry, reattaches at $\nu_b$, that is, is congruent with the already defined flowfield. According to the chain rule, the physical complex velocity has to satisfy the equation

$$\frac{dw}{dz} = \frac{dw}{d\nu}\frac{d\nu}{dz}$$

and, according to the previously defined mapping, is also expressed by the $\sigma = g(\nu)$ function Eq. (1). The following differential equation is thus found:

$$\frac{dz}{d\nu} = \frac{dw/d\nu}{g(\nu)}$$

The integral

$$z_0 = \int \frac{dw/d\nu}{g(\nu)}\, d\nu$$

computed along the real axis of the $\nu$ plane, provides the shape of the wall, with a length scale defined by the ratio $q_\infty/Q_\infty$.

It is necessary to note that the vortex location $z_V$ is part of the inverse solution. As a consequence, the vortex equilibrium is not assured and the absence of adverse pressure gradient is not rigorously guaranteed for the steady flow configuration. Nevertheless, as shown next, the steady solution slightly differs from the present inverse solution and the requirement of a favorable pressure gradient is attained with good approximation.

The cavity designed by the hodograph method is not optimal because viscous effects are not taken into account. Nevertheless, they are good candidates for hosting a steady solution with closed streamlines of the RANS equations. This solution indeed exists for the laminar case in the limit of the Reynolds number going to infinity [11].

## III.   Single Vortex Model

The vortex, as mentioned, is not in equilibrium. To evaluate the actual inviscid velocity distribution in the cavity, we developed analytical as well as numerical tools. The former are used to validate the latter in simpler geometries.

In the single vortex model, the recirculating region is described by a point vortex, otherwise the flow is potential. The circulation and the position of the vortex are obtained by satisfying the Kutta condition at the cavity edge as well as by imposing the equilibrium conditions of the vortex.

### A.   Analytical Solution: Indefinite Wall

The problem is posed as a direct problem, that is, the flow configuration, vortex location equilibrium, and stability are determined for given body shape. The method of solution is based on conformal mapping. The physical complex $z$ plane, being $z = x + iy$, is shown in Fig. 4. The flow region, bounded by two horizontal straight lines which extend to infinity and are connected by a half-circle, is mapped on the interior of the unit circle of $\mu$ plane by means of a chain of transformations.

The mapping

$$\zeta = \frac{z - i}{-iz + 1}$$

transforms the flow domain onto the interior of a cusped closed line of $\zeta$ plane, which is in turn mapped onto a regular curve of $\sigma$ plane by the transformation

$$\sigma = \sqrt{\zeta + i}$$

The mapping

$$\lambda = \frac{\sigma - \sigma_b}{-\sigma_b}$$

brings the centroid $\sigma_b$, the regular curve obtained on the $\sigma$ plane, onto the origin of $\lambda$ plane and rescales the closed line. Finally, the Theodorsen–Garrick mapping gives the relationship between the interior of the unit circle of the $\mu$ plane and the flowfield image of the $\lambda$ plane:

$$\lambda = \mu \exp \sum_{n=0}^{\infty}(a_n - ib_n)\mu^n \qquad (2)$$

Once the series in Eq. (2) is truncated to a suitably large number $N$ of terms, the $a_n$, $b_n$ coefficients can be determined according to a trial-and-error process by enforcing the correspondence between the $\mu$ and $\lambda$ planes.

The complex potential $w(\mu)$ can be defined on the transformed $\mu$ plane as

$$w = i\frac{M\exp(i\varphi_\infty)}{\mu - \mu_\infty} + \frac{\gamma}{2\pi i}\log\left(\frac{1}{\mu - \mu_v} - \frac{1}{\mu - \bar{\mu}_v}\right) \qquad (3)$$

where $M$ is the strength of a doublet responsible for the asymptotic flow at infinity on physical $z$ plane, $\mu_\infty$ is the image of the point at infinity of the physical plane, $\varphi_\infty = \arg(\mu_\infty)$, $\gamma$ is the trapped vortex circulation, $\mu_v$ its location, and $\bar{\mu}_v = 1/\mu_v^*$, with ($^*$) denoting complex conjugation.

The doublet strength $M$ is related to the physical velocity at infinity $q_\infty$, in fact, being the complex velocity on the physical plane
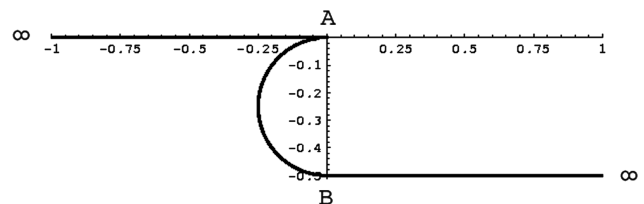
$$\frac{dw}{dz} = \frac{dw/d\mu}{dz/d\mu}$$

it is



**Fig. 4   Physical $z$ plane.**

$$q_\infty = \lim_{\mu \to \mu_\infty} \frac{dw/d\mu}{dz/d\mu} = -\frac{M}{2}\left|\frac{dz}{d\mu}\right|_{\mu_\infty}$$

The $(\gamma, \mu_v)$ vortex circulation and location are determined by enforcing the Kutta condition and the vortex equilibrium condition. The Kutta condition requires that, at the trailing-edge image $\mu = \mu_A$, it is

$$\left(\frac{dw}{d\mu}\right)_{\mu_A} = 0$$

and the vortex equilibrium condition according to the Routh rule (see, for instance, [25] and references therein) is

$$\dot{\mu}_v^\star - \frac{\gamma}{4\pi i}\frac{d}{d\mu}\left(\log\frac{dz}{d\mu}\right)_{\mu=\mu_v} = 0$$

with

$$\dot{\mu}_v^\star = -i\frac{M\exp(i\varphi_\infty)}{(\mu_v - \mu_\infty)^2} - \frac{\gamma}{2\pi i}\frac{1}{\mu_v - \bar{\mu}_v}$$

Figure 5 shows the streamline pattern, and Fig. 6 shows the flow velocity at the wall.

## B. Numerical Solution

In this section, we describe a numerical method to compute the flow due to a point vortex inside a cavity of arbitrary geometry. The numerical solution is obtained by means of Green's functions. The same approach is at the basis of the technique that we will use for the integration of the Prandtl–Batchelor model. Here, we validate this
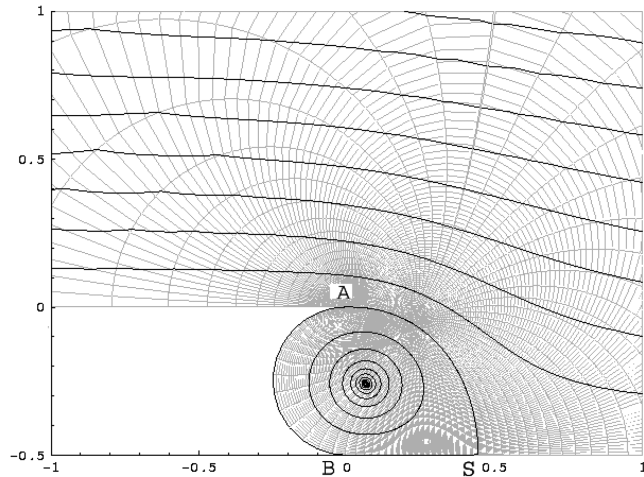


**Fig. 5   Streamline pattern. In gray, the image of a polar grid on the interior of the $\mu$-plane unit circle.**
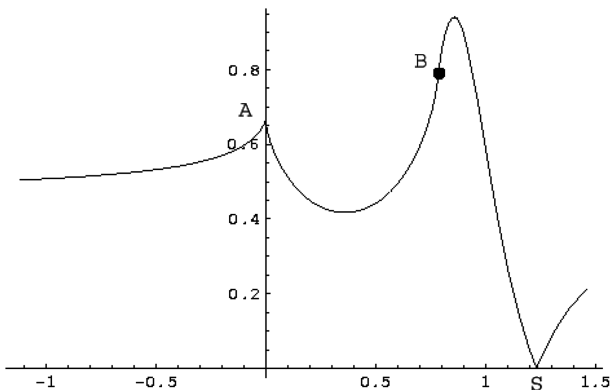


**Fig. 6   Flow velocity at the wall.**

approach by comparing it to the analytical solution determined in the previous section.

Let us define $\Omega$ as the rectangular domain where the flow is taking place, and let $\Gamma_d$, $\Gamma_u$, $\Gamma_l$, and $\Gamma_r$ be the lower, upper, left, and right boundaries. The nonlinear problem to be solved to find the equilibrium position of a point vortex immersed in a given cavity flow is the following:

$$\Delta\psi = \gamma\delta(x - x_v, y - y_v) \quad \text{in } \Omega \tag{4}$$

$$\psi = 0 \quad \psi \in \Gamma_d; \qquad \psi = U_\infty h \quad \psi \in \Gamma_u \tag{5}$$

$$\frac{\partial\psi}{\partial n} = 0 \quad \psi \in \Gamma_l; \qquad \frac{\partial\psi}{\partial n} = 0 \quad \psi \in \Gamma_r \tag{6}$$

$$\dot{x}_v = 0 \qquad \dot{y}_v = 0 \tag{7}$$

where $\psi$ is the stream function, $x_v$ and $y_v$ are the vortex coordinates, and $h$ is a characteristic length. Let

$$\psi = \psi_0 + \frac{\gamma}{2\pi}[\psi' + \log\sqrt{(x - x_v)^2 + (y - y_v)^2}] \tag{8}$$

The auxiliary function $\psi_0$ satisfies

$$\Delta\psi_0 = 0 \quad \text{in } \Omega \tag{9}$$

$$\psi_0 = 0 \quad \psi_0 \in \Gamma_d; \qquad \psi_0 = U_\infty \quad \psi_0 \in \Gamma_u \tag{10}$$

$$\frac{\partial\psi_0}{\partial n} = 0 \quad \psi_0 \in \Gamma_l; \qquad \frac{\partial\psi_0}{\partial n} = 0 \quad \psi_0 \in \Gamma_r \tag{11}$$

and if $\psi'$ is chosen so that

$$\Delta\psi' = 0 \quad \text{in } \Omega \tag{12}$$

$$\psi' = -\log\sqrt{(x - x_v)^2 + (y - y_v)^2} \quad \psi' \in \Gamma_d \tag{13}$$

$$\psi' = -\log\sqrt{(x - x_v)^2 + (y - y_v)^2} \quad \psi' \in \Gamma_u \tag{14}$$

$$\frac{\partial\psi'}{\partial n} = -\frac{\partial}{\partial n}[\log\sqrt{(x - x_v)^2 + (y - y_v)^2}] \quad \psi \in \Gamma_l \tag{15}$$

$$\frac{\partial\psi'}{\partial n} = -\frac{\partial}{\partial n}[\log\sqrt{(x - x_v)^2 + (y - y_v)^2}] \quad \psi \in \Gamma_r \tag{16}$$

then the function $\psi$ satisfies the original problem Eqs. (4–6) with the required singularity at $(x_v, y_v)$. It is seen that the function $\psi'$ is the preliminary Green's function [26] and $\psi' + \log\sqrt{(x - x_v)^2 + (y - y_v)^2}$ is the Green's function of the operator $\Delta$ with boundary conditions Eqs. (5) and (6).

We are now left with the problem of finding the equilibrium position and the vortex intensity $\gamma$. The vortex intensity is determined by imposing that the separation point is at the cusp. This means that the velocities on the cusp sides are parallel and equal in modulus. Let us denote by $(\partial\psi/\partial n)^+$ and $(\partial\psi/\partial n)^-$ the tangent velocities on the cusp sides. Then, since

$$(\partial\psi/\partial n)^+ = -(\partial\psi/\partial n)^- \tag{17}$$

and in view of Eq. (8), we have a linear equation in $\gamma$. Hence, given $(x_v, y_v)$, the solution $\psi$ is uniquely determined.

On the other hand, the vortex velocity is

$$\dot{x}_v = \frac{\partial}{\partial y}(\psi_0 + \gamma\psi')|_{(x_v,y_v)} \qquad \dot{y}_v = -\frac{\partial}{\partial x}(\psi_0 + \gamma\psi')|_{(x_v,y_v)} \quad (18)$$

and the solution is obtained when $(x_v, y_v)$ are such that the preceding velocity is zero. The solution is obtained by Newton's method.

It is noted that, although the solution is found iteratively, the function $\psi_0$ is determined once for all. In addition, to obtain $\psi'$, the discrete operator needs to be inverted one time because only the right-hand side is changing from one iteration to another.

As an example, we compare the numerical results to the analytical solution previously found. The simulation was performed over a nonstructured grid of 19,444 triangles using $P2$ continuous finite elements. The numerical results compare well with the analytical solution, although they were obtained in a finite domain: the vortex nondimensional coordinates are for both $x_v = 0.257$, $y_v = -0.036$ taking the origin at the center of the cavity with a radius $R = 1$. Likewise, for the nondimensional vorticity with $U_\infty = 1$, both methods give $\gamma = -8.6$.

## IV.  Prandtl–Batchelor Model

We now consider a more sophisticated model, as compared to a point vortex, to describe the recirculating region. Consider a two-dimensional inviscid and steady flow. In a nonseparated region, all the streamlines come from infinity. The vorticity is constant along the streamlines, and its distribution across the streamlines can be determined from the boundary conditions at infinity. In steady separated flows, streamlines form closed contours in the eddy. Therefore, the vorticity on closed streamlines cannot be determined from the boundary conditions. Instead, the distribution of vorticity is governed by viscous effects, however small they are, as demonstrated by the Prandtl–Batchelor theorem. In the limit of Reynolds number tending to infinity, it is shown that the correct inviscid limit for a recirculating region, that is, a region with closed streamlines, is not a point vortex but is given by a distributed region of constant vorticity and given Bernoulli constant jump across the separatrix.

The Prandtl–Batchelor model for our problem is set as follows:

$$\Delta\psi = -\omega H(-\psi) + \beta\delta(\psi) \quad \text{in } \Omega \qquad (19)$$

$$\psi = 0 \qquad \psi \in \Gamma_d; \qquad \psi = U_\infty \qquad \psi \in \Gamma_u \qquad (20)$$

$$\frac{\partial\psi}{\partial n} = 0 \qquad \psi \in \Gamma_l; \qquad \frac{\partial\psi}{\partial n} = 0 \qquad \psi \in \Gamma_r \qquad (21)$$

where $\omega = \nabla \times \mathbf{U}$, $H(\cdot)$ is the Heaviside function, $\delta(\psi) = \partial H(\psi)/\partial\psi$, and $\beta$ is the jump in the Bernoulli constant. This problem is highly nonlinear and of sensitive numerical solution. It was solved only in the presence of no or very simple geometries by explicitly determining the geometry of the separatrix, that is, the dividing streamline between the vortex core and the external flow. In the following, we solve this problem by a finite element discretization.

### A.  Numerical Solution

The solution method is based on the Schauder fixed-point theorem. Let

$$\psi = \psi_0 + \omega\psi' \qquad (22)$$

where $\psi_0$ is defined as in the point-vortex case, and $\psi'$ satisfies

$$\Delta\psi' = 0 \quad \text{in } \Omega - \Omega_v \qquad (23)$$

$$\Delta\psi' = 1 + \frac{\beta}{\omega}\delta_\epsilon(\psi) \quad \text{in } \Omega_v \qquad (24)$$

$$\psi' = 0 \qquad \psi' \in \Gamma_d; \qquad \psi' = 0 \qquad \psi' \in \Gamma_u \qquad (25)$$

$$\frac{\partial\psi'}{\partial n} = 0 \qquad \psi' \in \Gamma_l; \qquad \frac{\partial\psi'}{\partial n} = 0 \qquad \psi' \in \Gamma_r \qquad (26)$$

where $\Omega_v \subset \Omega$. The function $\delta_\epsilon(\cdot)$ is a regularization of the Dirac function. In particular, we took $\delta_\epsilon(\psi) = \exp(-\psi^2/\epsilon^2)/(\epsilon\sqrt{2\pi})$, and it can be shown that

$$\lim_{\epsilon\to 0}\delta_\epsilon(\psi) = \delta(\psi)$$

The vorticity $\omega$ is found by imposing the Kutta condition at the sharp edge, whereas the ratio $\beta/\omega$ is to be determined by boundary-layer considerations, and here it is assumed as given.

Let $\Omega_v$ be given at iteration zero, and solve for $\psi'$. Then $\Omega_v$ at iteration one is the support of $H(-\psi)$, that is, we have

$$\Delta\psi^{n+1} = -\omega[H(-\psi^n) + \beta/\omega\delta(\psi^n)] \quad \text{in } \Omega \qquad (27)$$

with the appropriate boundary conditions. This iteration has fixed points. Again, the discrete operator matrix relative to the equations for $\psi'$ are inverted only once, and then the right-hand side is varied from one iteration to another.

We validate our method by comparing it with the so-called Sadovski vortex. The Sadovski vortex is a soliton solution of Eqs. (19–21) in a rectangle. For a rectangle height of one, velocity at infinity one, $\beta = 0$, and, for example, total circulation of 2.5, we find $\omega = -16.8$, whereas Chernyshenko [27] found $\omega = -17.0$. The slight difference in the results is due to the different grid resolutions, as well as to the order of accuracy of the approximation; third order in the present case. The numerical scheme was implemented using a high-level language providing finite elements subroutines.**

### B.  Design of Trapping Cavity Geometries

We now have a method to design cavities that are not optimal but that are likely to host a vortical flow. In practice, this flow will be unstable because of secondary separations in the cavity and of Kelvin–Helmholtz instabilities developing at the interface between the external flow and the cavity flow. As an example, we show the geometries obtained for several configurations of the velocity profile in the hodograph plane. As the circular arc through the points $E$, $B$, and $A$ in Fig. 2 tend to close, that is, $E \equiv A \neq B$, the cavity in the physical plane will get closer and closer to a circle. The geometries are shown in Fig. 7. They have been designed by taking the argument of point $A$ on the unit circle of the hodograph plane ($\vartheta_A$) at 20, 30, 40, and 50 deg, respectively. The cavities have been normalized so that the distance computed along the streamline connecting points $A$ and $B$ is the same for all cavities.

The flow over cavities $\text{cav}_{20}$ and $\text{cav}_{50}$ was simulated by both the point-vortex model and the Prandtl–Batchelor model with $\beta = 0$. Overall, the solution obtained by the Batchelor model is very similar to that obtained by a point-vortex model (see Figs. 8 and 9). In the figures, $s$ is the curvilinear coordinate starting at point $x = -2$. The cusp is located at $s = 2$. The rear stagnation point corresponds to the minimum of the velocity profile. If a large enough number of plot points were used, this minimum would of course be zero. Between the cusp and the rear stagnation point, the flow is in the direction of decreasing $s$. As compared with the prediction of the point-vortex model, the unfavorable pressure gradient regions taking place inside the cavity predicted by the Prandtl–Batchelor model inside the cavity are less severe for both cavities. The position of the rear stagnation points predicted by the two models is very close. Finally, we note that the overall flow speed inside the cavity tends to a constant velocity over the wall, in accordance with the design criteria.

The main point is now to see if the Batchelor model, with an appropriate jump in the Bernoulli constant, gives a good
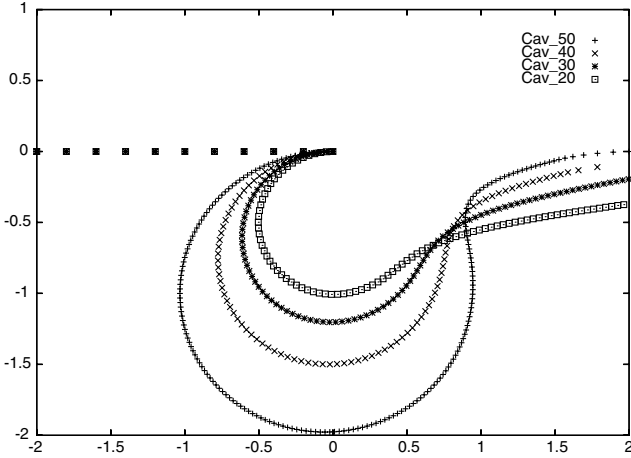
---

**Data available online at http://www.freefem.org/.

**Fig. 7   Profiles obtained for different values of $\vartheta_A$.**
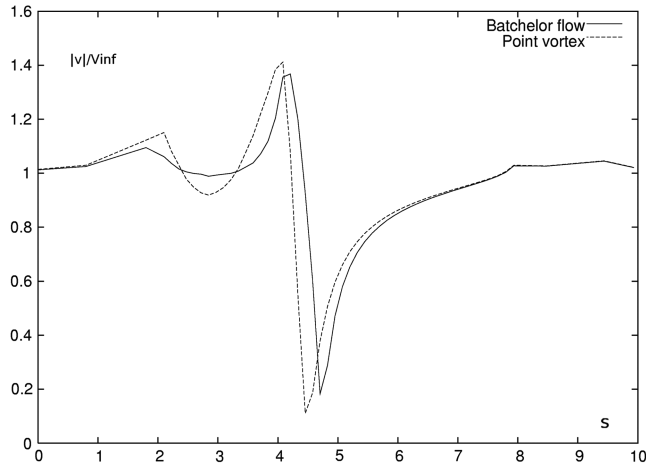


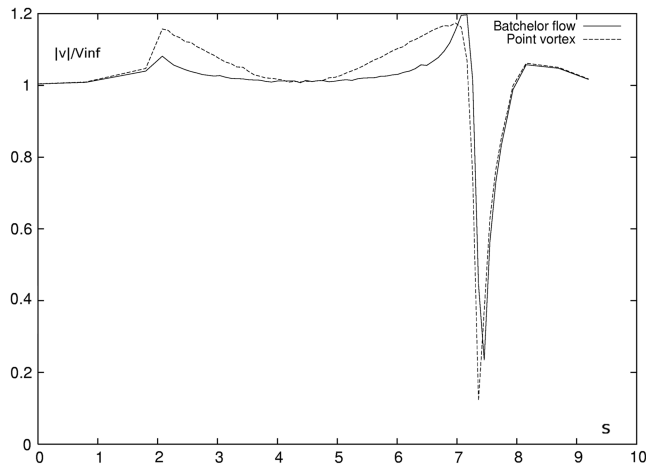**Fig. 8   Prandtl–Batchelor flow and potential solution, cav$_{20}$.**



**Fig. 9   Prandtl–Batchelor flow and potential solution, cav$_{50}$.**

representation of the pressure distribution inside the cavity as compared with a more sophisticated and, hopefully, more accurate model, like the RANS equations system.

## V.   Reynolds-Averaged Navier–Stokes Simulations

The aim of this section is to reproduce the flows described in the previous sections by means of an even more detailed physical model, which will hopefully provide us with a reference solution to be used for evaluating the simplified models.

In [13,14], it is argued that the incompressible, isothermal, steady RANS system of equations can be assumed with good approximation as the governing physical/mathematical model. Besides already known limitations of the RANS approach, the additional problem arising in the simulation of cavity flows is that there is no specific turbulence model available in literature for treating turbulent cyclic boundary layers. Nonetheless, in [13,14], the most popular turbulence models, such as the $k$-$\epsilon$ and $k$-$\omega$ models, were used with good success in the reproduction of trapped vortex experimental data.

Therefore, a pragmatic approach is followed in this section. By using slightly different numerical methods but similar turbulence models, we first demonstrate that, with a commercial flow solver (FLUENT), it is possible to set up a numerical procedure that provides coherent results with those obtained in [13,14], and with respect to the available experimental data.

After that, this numerical setup will be used to predict the flowfield about one of the cavity shapes whose design procedure was illustrated in the previous sections. Finally, the results obtained with the RANS approach will be compared with the Prandtl–Batchelor model results.

### A.   Boundary-Layer Characteristics

The adoption of a turbulent viscous flow model poses the difficulty of prescribing a realistic boundary-layer profile running over the vortex trapping cavity. Within the incompressible, isothermal, steady RANS flow model, both the density $\rho$ and dynamic viscosity $\mu$ are assumed to be constant. In such a case, our flow problem is governed by two nondimensional numbers, namely the ratio $\delta/L$ between the incoming boundary-layer thickness $\delta$ and the cavity opening $L$ (i.e., the length of the streamline going from points $A$ and $B$ of Fig. 1), and the Reynolds number defined as follows:

$$Re_\delta = \frac{U_e \cdot \delta}{\nu} \qquad (28)$$

where $U_e$ is the velocity at the boundary-layer edge and $\nu$ is the kinematic viscosity. All these boundary-layer-based quantities will be evaluated at some distance upstream of the cavity. Furthermore, it is assumed that, whatever the Reynolds number considered, a turbulent boundary layer (of specified thickness $\delta$) runs over the vortex trapping cavity. This is based on a first approximation hypothesis that the cavity is placed downstream the maximum thickness of the airfoil and, therefore, after the transition point from laminar to turbulent flow. It is assumed that, at the left boundary of the computational domain, that is $x = -2$, such boundary layer has a velocity profile described by a piecewise law, according to the formulation proposed in [28]:

$$u(y) = \frac{u_L}{\delta_L}y \qquad y \leq \delta_L \qquad \frac{u(y)}{U_e} = \left(\frac{y}{\delta}\right)^{\frac{1}{7}} \qquad \delta_L \leq y \leq \delta$$

$$\frac{u(y)}{U_e} = 1 \qquad y > \delta \qquad v(y) = 0 \quad \forall\ y \qquad (29)$$

where the well-known 1/7 power law is used, which approximates the velocity profile of a zero pressure gradient turbulent boundary layer over a flat plate [29]. In Eq. (29), $u$ and $v$ are the streamwise and wall normal velocity components, respectively, and $y$ is the abscissa normal to the wall. Moreover, the current formulation takes into account the linear behavior of the velocity profile in the thin laminar sublayer of thickness $\delta_L$ existing close to the wall; $u_L$ being the velocity value at the edge of this small region. For assigned $Re_\delta$ and inlet boundary-layer thickness $\delta$, the following additional relations [28] are used to determine both $u_L$ and $\delta_L$:

$$\frac{\delta_L}{\delta} = \left(\frac{158}{Re_\delta}\right)^{0.875}; \qquad \frac{u_L \delta_L}{\nu} = 158 \qquad (30)$$

The preceding relations have been derived in such a way to satisfy the well-known skin-friction law [29]:
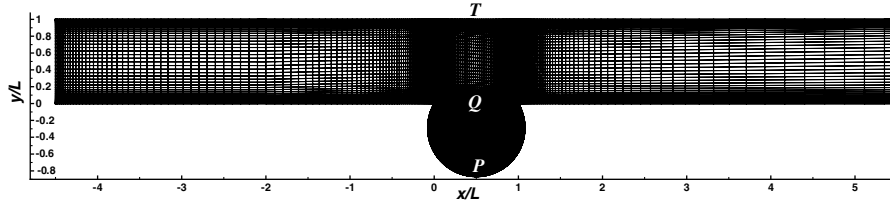
**Fig. 10   Computational grid inside the rectilinear channel with circular vortex cell. $L$ is the cavity opening.**

$$C_f = \frac{0.045}{(Re_\delta)^{1/4}} \tag{31}$$

The turbulence quantities associated with the incoming boundary layer can be specified in a similar way. In particular, we assume that the turbulent kinetic energy (per unit mass) is defined by the following piecewise law:

$$k(y) = \frac{k_L}{\delta_L} y \quad 0 \le y \le \delta_L \quad k(y) = k_L + \frac{k_e - k_L}{\delta - \delta_L}(y - \delta_L)$$
$$\delta_L \le y \le \delta \quad k(y) = k_e \quad y > \delta \tag{32}$$

The value of $k_L$ can be determined by using the log-layer relations:

$$k_L = \frac{u_\tau^2}{C_\mu^{1/2}} \tag{33}$$

with $u_\tau = U_e \sqrt{C_f/2}$ being the friction velocity and $C_\mu = 0.09$. Moreover, by the knowledge of the freestream turbulence intensity $I_t$, the turbulent kinetic energy at the boundary-layer edge can also be estimated:

$$k_e = \frac{3}{2}(I_t \cdot U_e)^2 \tag{34}$$

With the available profile of $k$, the profile for the dissipation per unit mass $\epsilon$ can be derived from the following expression [30]:

$$\epsilon(y) = \frac{C_\mu^{3/4} \cdot k(y)^{3/2}}{l} \tag{35}$$

where $l$ is the Prandtl's mixing length, which can be modeled as $\min(0.41y, 0.085\delta)$. Similarly, the profile for the specific dissipation rate $\omega$ can be derived according to

$$\omega(y) = \frac{\epsilon}{0.09 \cdot k} \tag{36}$$

A similar but more simplified strategy has been adopted in [13] to include the effect of the incoming boundary-layer thickness on the flowfield inside a circular vortex cell.

**B.   Selection of a Turbulence Model**

The commercial code we used (FLUENT) solves the RANS equations on hybrid grids by means of a finite volume method. The flow equations are solved simultaneously, except those related to turbulence modeling, which are solved sequentially. A preconditioning method is used that modifies the time-derivative terms appearing in the governing equations, such that the eigenvalues of the equation system always remain well conditioned with respect to the convective and diffusive time scales. The viscous terms are approximated by a central finite difference formula and are second-order accurate in space. A standard upwind, flux-difference splitting scheme is used to reconstruct the inviscid flux vector at cell faces. Furthermore, an Euler implicit discretization combined with a Newton-type linearization of the fluxes is used in the pseudotime to produce a linearized system of algebraic equations. Such an equation system is solved using a point Gauss–Seidel scheme, in conjunction with an algebraic multigrid method to enhance convergence, adapted for coupled sets of equations.

In this section, we compare the performance of two turbulence models when applied to the simulation of the flow in a two-dimensional plane channel with a circular cavity. They were selected on the basis of a preliminary investigation by comparing the simulations to experimental results. Experimental data are available from literature [13,14]. The problem geometry and the computational grid used are shown in Fig. 10. Such grid is made of about 40,000 quadrilateral cells and was built by placing 98 streamwise cells upstream of the circular cavity, 79 cells along both the cavity opening (i.e., between points $x/L = 0$ and $x/L = 1$) and in the transverse direction, 69 cells downstream of the cavity, and 237 cells along the cavity periphery. Furthermore, the first layer of cells close to the solid walls is placed at a distance such to ensure a $y^+$ value close to unity to properly account for the viscous sublayer within the adopted low-Reynolds number turbulence models formulation.

Moreover, such mesh density was demonstrated to be adequate in providing mesh-independent solutions. The numerical boundary conditions used to carry out the simulations include 1) prescribed velocity and turbulence profiles at the inflow boundary, according to the procedure described in Sec. V.A; 2) no-slip conditions at solid walls; and 3) zero normal gradient of flow variables at the outflow boundary.

The two flow conditions considered in the simulations are summarized in Table 1. In each case, the nondimensional boundary-layer thickness $\delta/L$ is evaluated at $x/L = -1.06$, according to the experimental definition [13,14]. Moreover, the turbulence intensity in the flow core is fixed to $I_t = 0.015$ in accordance with experimental measurements.

To match the experimental boundary-layer thickness, a sequence of trial-and-error simulations have been performed. A tentative $\delta_{\text{in}}/L$ at the inflow was assigned and the boundary-layer thickness at $x/L = -1.06$ was evaluated afterward.

For the sake of brevity, in the present work, we show only the numerical results carried out by using the well-known Spalart–Allmaras [31] (S-A) turbulence model and the shear-stress transport (SST) $k - \omega$ turbulence model [32]. In particular, we refer to the S-A model with the modification proposed in [33], which also includes the effects of the mean strain in the turbulence production term, otherwise depending solely on the mean rate of rotation. In this slightly modified model, the eddy viscosity production is limited in those flow regions where the measure of vorticity exceeds that of strain rate. A typical case where such modification takes place is in vortical flows, particularly in the core region of a vortex, where pure rotation occurs and is experimentally observed (e.g., see [13,34]) that the turbulence should be suppressed there.

As already highlighted earlier, the subject of establishing a turbulence model to be used for such kinds of simulations is out of the scope of the present work, and we will limit our attention in verifying whether existing turbulence models produce results that are physically reasonable and that reflect what has been observed experimentally.

**Table 1   Values of $Re_\delta$ and nondimensional boundary-layer thickness $\delta/L$ used in the numerical simulations**

| Case | $Re_\delta$ | $\delta/L$ |
|---|---|---|
| 1 | 5360 | 0.04 |
| 2 | 13,400 | 0.1 |

Figure 11 shows both the streamlines and the velocity magnitude contours obtained by the two turbulence models for the case 2 of Table 1. As can be observed, there is a substantial difference between the two solutions. In particular, from the velocity contours, it appears that the S-A model provides a faster vortex, which is also different in shape if compared with the SST solution. In particular, by looking at the separatrix (i.e., the streamline connecting the two cavity edges), it appears that the S-A model predicts a more convex streamline pattern than the SST model. As a consequence, the streamline patterns inside the large-scale vortex are also different: the S-A model predicts almost circular streamlines, whereas the SST model predicts streamline patterns of elliptical shape. In both cases, a secondary separation occurs inside the cavity, in correspondence of the upstream edge, which was already observed in [13,14] for two-dimensional RANS simulations, but not observed in either three-dimensional simulations nor experiments.

To quantitatively compare the numerical results with the available experimental data, in Fig. 12, we report the $x$-velocity profiles along the cavity vertical centerline. Despite the fact that the two solutions

provide an almost linear behavior of the velocity in the cavity, which is in agreement with the Prandtl–Batchelor theory, the two models predict a quite different rotation velocity of the trapped vortex. Moreover, quite different velocity profiles in the shear layer can also be observed. As suggested by Fig. 12, it appears that the SST model results are in remarkable accordance with the experiments, whereas the S-A model provides a vortex rotating too fast and an overall unsatisfactory agreement with the measurements. In particular, the SST model performs quite well for the low $Re_\delta$ case: the velocity profile in the bottom region of the cavity is captured with very good accuracy up to the vortex center. It is also worth noting that the so-called jet effect, which can be recognized by the presence of an inflection point between cavity bottom and its center, is very well reproduced by the SST numerical solution. Above the vortex center, some differences with the experimental data can be observed, particularly in the upper part of the cavity where the experimental data indicate a slower motion. In [14], it is argued that such discrepancy is due to the assumed bidimensional flow model in computations, whereas a weak three-dimensional character of the
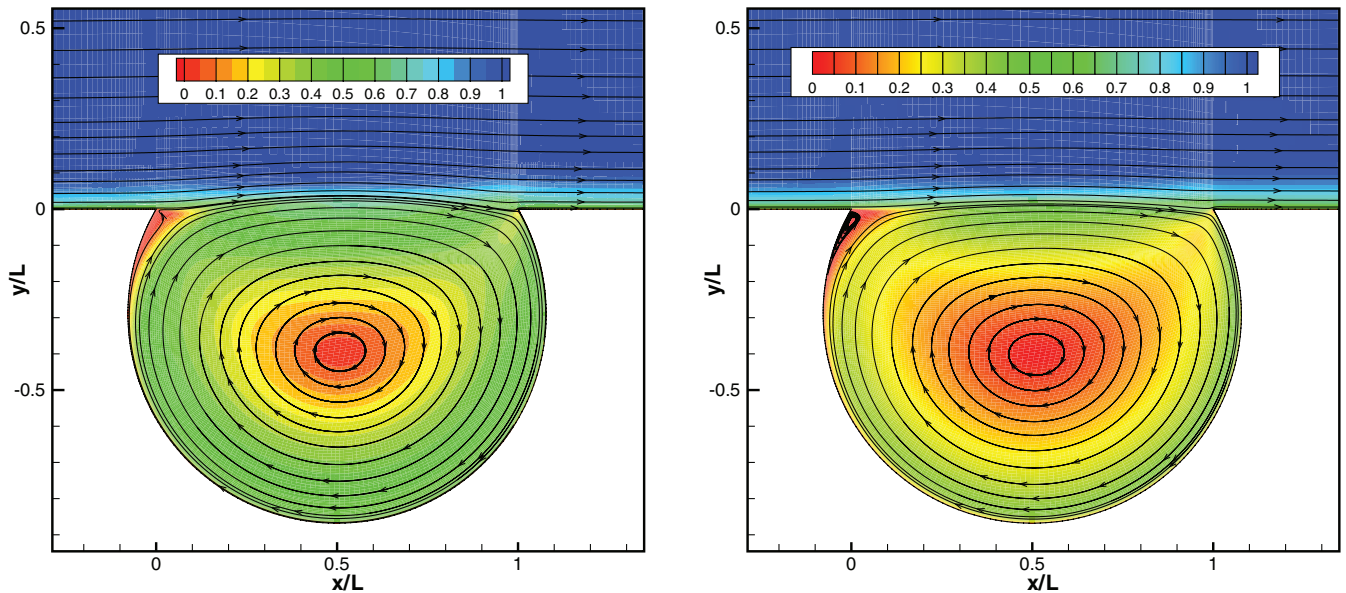


Fig. 11    Streamlines and contours of nondimensional velocity magnitude $V/U_e$ obtained by S-A model (left) and $k$-$\omega$ SST model (right). Case 2 of Table 1.
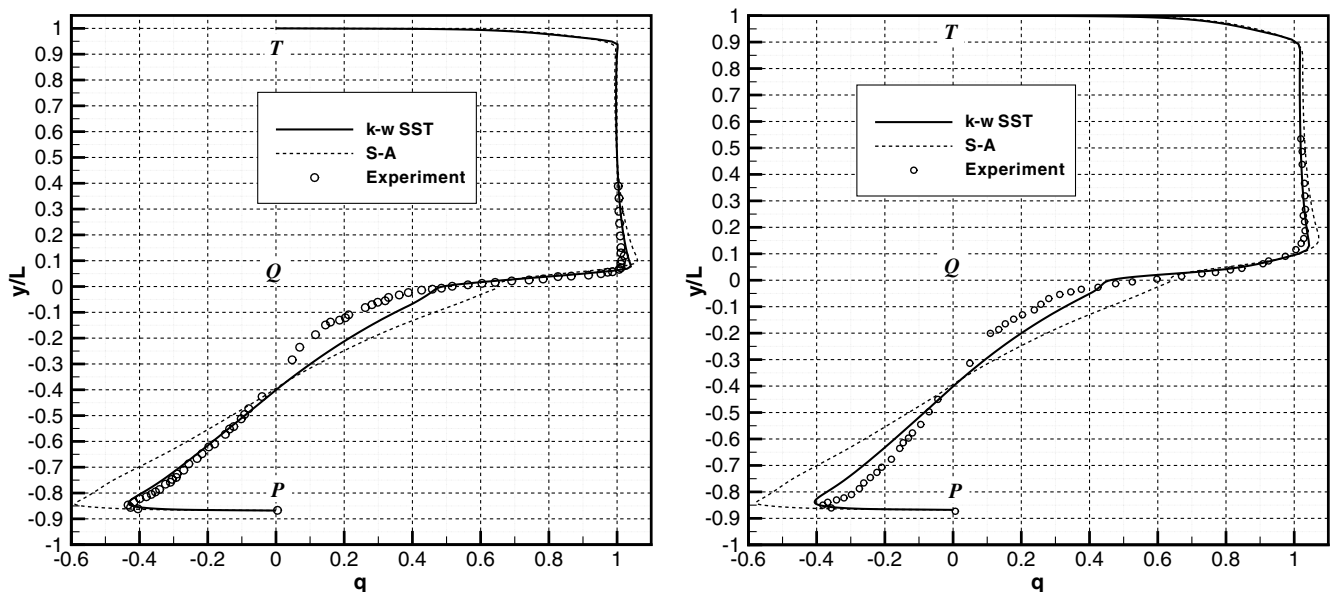


Fig. 12    Velocity profiles along the cavity centerline; $q(y) = u(0.5y)/u(-1.06, 0.5)$. Case 1 (left) and case 2 (right) of Table 1. Points $P$, $Q$, and $T$ are relative to Fig. 10.

flow was observed in the experiments. As a demonstration of this, in [13], it is shown that, within the framework of a three-dimensional RANS simulation, such disagreement is rather reduced. In the higher $Re_\delta$ case, a slightly reduced agreement with the experimental data can be observed as, overall, the SST model provides a bit faster vortex with respect to the experiment. Also, the jet effect at the bottom wall seems to be not properly reproduced by the numerical simulation. However, the same discrepancies with the experimental data has been obtained in [13,14] for the same flow condition, in the framework of both two- and three-dimensional simulations.

In Fig. 13, the profiles of the absolute vorticity along the cavity centerline are compared with the experimental data for case 2 of Table 1. As already observed, the S-A model provides a vortex that is too fast and hence too-high vorticity in the cavity with respect to both the experiment and the SST simulation. This latter model is in a better agreement with the experiment, although, for this flow condition, it provides a slightly faster vortex with respect to the experiment. This was already noted earlier, in commenting on the velocity profiles obtained for such test case.

By looking at the velocity profile obtained by the SST model for the low $Re_\delta$ test case, there is a reasonable confidence that the agreement with the measured vorticity improves remarkably for such flow condition. Unfortunately, such experimental data are unavailable from the literature.

As a final comparison of the numerical results with the experimental data, we show in Fig. 14 the profile of a nondimensionalized static pressure (so-called reduced pressure) along the cavity vertical centerline. Such pressure is defined as $p_{\text{reduced}} = (p - p_m)/(p_c - p_m)$, with $p$ being the local static pressure, $p_m$ the static pressure in the center of the large-scale vortex, and $p_c$ as the static pressure in the middle of the channel at $x/L = 0.5$. As can be observed, such profiles look very similar for both models and, overall, there is a reasonable agreement with the experimental data.

The results shown in this section suggest that RANS simulations, provided that a suitable numerical and modeling setup is chosen, can be successfully adopted for simulating trapping cavity flows. In the next section, we employ such a numerical setup to carry out simulations for one of the cavities designed by the hodograph method.

### C.  Reynolds-Averaged Navier–Stokes Analysis of a Vortex Trapping Cavity

The inviscid flow calculations performed in Sec. IV.B show that reduced adverse pressure gradients are present in the cavity, for all
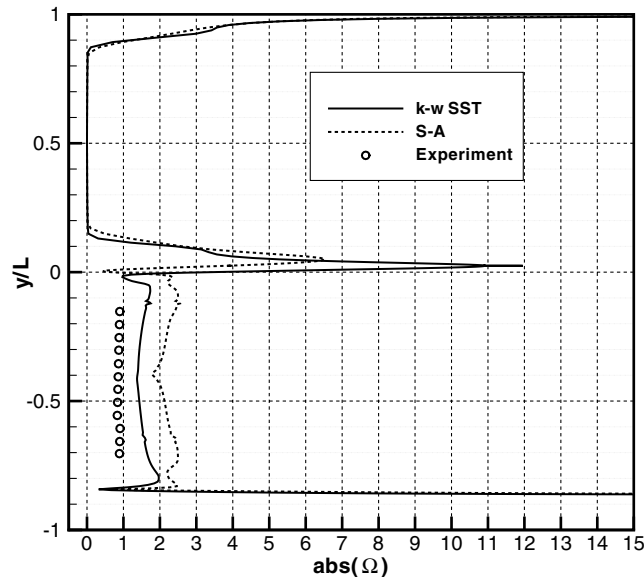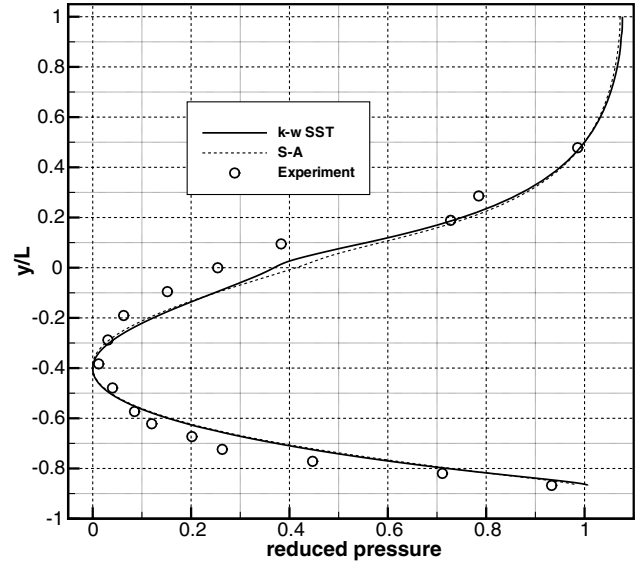


**Fig. 14   Profiles of reduced pressure along the cavity centerline. Case 2 of Table 1.**

cavity shapes, from $cav_{20}$ to $cav_{50}$. It was decided to carry out the RANS simulations for the $cav_{50}$ geometry, as it exhibits a weaker adverse pressure gradient and thus it most likely allows for the existence of a steady vortical solution without secondary separations.

#### 1.  Computational Domain and Grid

The considered computational domain is shown in Fig. 15, where the $cav_{50}$ geometry has been scaled to have a radius $R = 1$. It is worth noting that the current cavity shape is characterized by a rounded downstream edge, therefore, it is difficult to exactly define a measure of the cavity opening $L$. However, wherever the exact location of the downstream stagnation point will be, this cavity has the ratio $L/R \approx 1$, different from the circular cavity considered earlier, for which such ratio is about 1.73. The 2-D grid used for the computations is made up of approximately 27,000 quadrilateral cells and is shown in Fig. 16. Particular care was devoted to attain both a $y^+$ on the order of one in the first layer of cells close to solid walls and to ensure a proper resolution near the cusp, in the boundary layers and in the shear layer. Such mesh was demonstrated to be dense enough
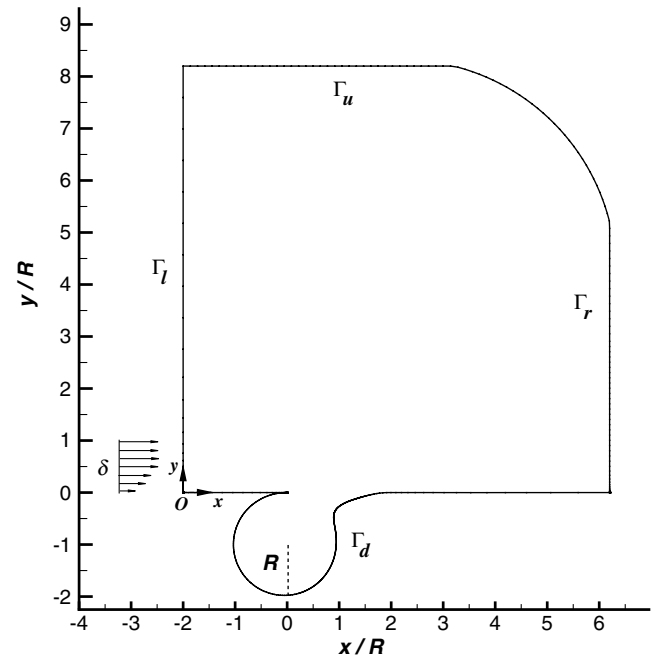


**Fig. 13   Profiles of absolute vorticity along the cavity centerline. Case 2 of Table 1.**



**Fig. 15   Cav50 geometry: sketch of the computational domain, incoming boundary-layer thickness $\delta$, and cavity radius.**
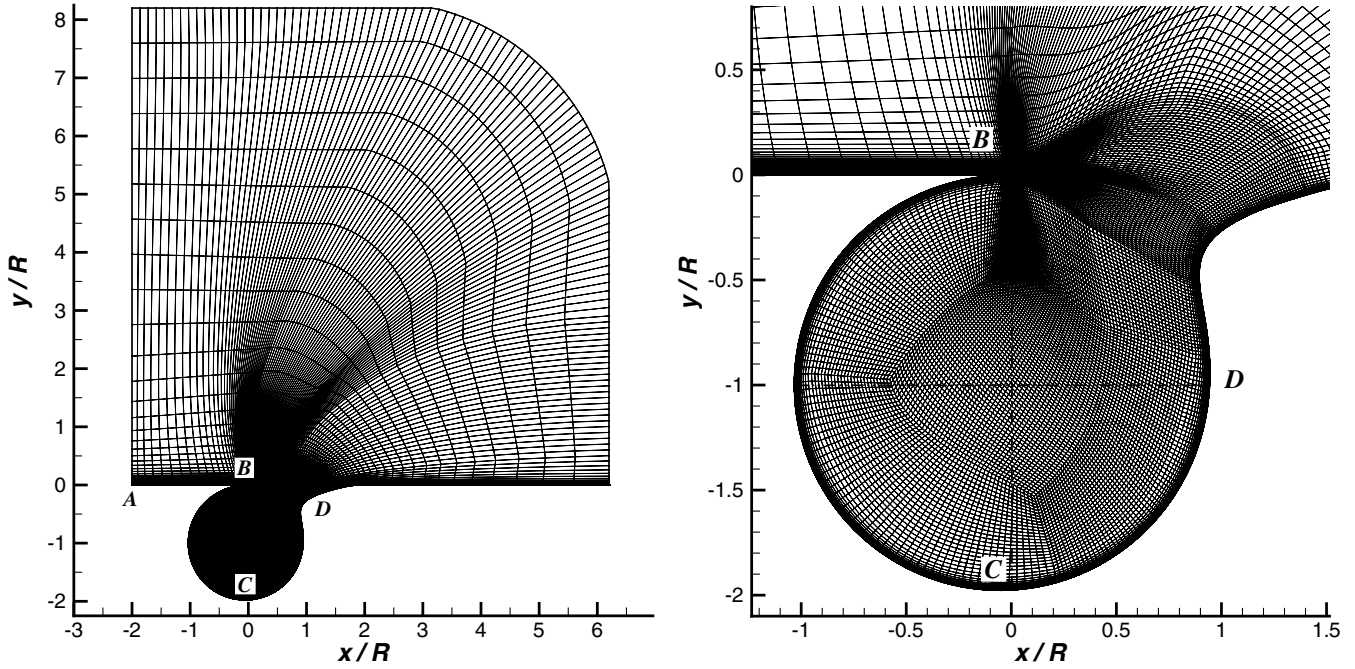
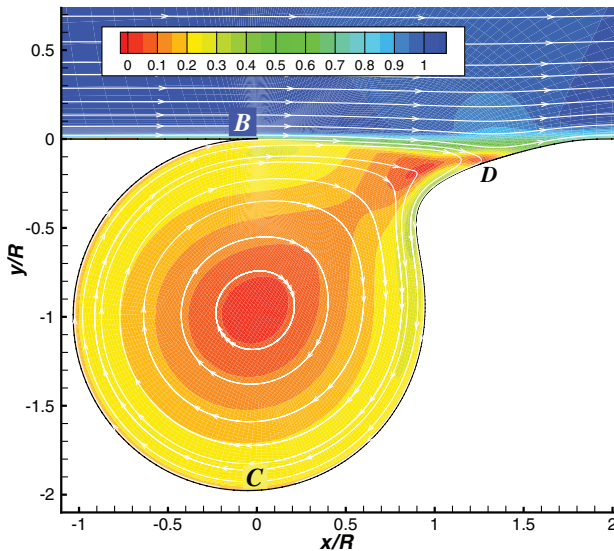Fig. 16 Computational grid around the cav50 geometry: overall layout (left) and zoom on the cavity (right).



Fig. 17 Velocity magnitude contours and streamline inside the cav50cavity. Case 1 of Table 1.

to provide grid-independent results by performing an additional simulation on a mesh of approximately 104,000 quadrilateral cells. The pressure coefficient along the cavity wall obtained on the latter mesh is superimposed on the pressure coefficient obtained with the 27,000 quadrilateral cells.

### 2. Flow Conditions

To have meaningful comparisons with the computations shown previously for the circular cavity case, the present analysis has been carried out for the same flow conditions summarized in Table 1. However, as already highlighted in the previous section, full flow similarity with the previous analysis cannot be achieved due to the absence of geometrical similitude. Different from what has been done in Sec. V.B, in this case, a zero normal gradient boundary condition has also been used on the top side of the computational domain shown in Fig. 15.

### 3. Results

Figure 17 shows the velocity contour and the streamline pattern of the flow inside the cav$_{50}$ cavity for case 1 of Table 1. As can be

observed, quite different flow behavior from the previously analyzed circular cavity case can be observed, especially around the downstream stagnation point. As a matter of fact, in this case, the downstream stagnation point location is not constrained by the cavity geometry and it is in a rather advanced position with respect to the vortex center. Because of this, and the asymmetrical cavity shape, the internal streamlines tend to curve quite a lot in the vicinity of the stagnation point. On the other hand, in the inner part of the cavity, the streamlines are almost circular in shape.

In Fig. 18, the velocity profiles along the cavity centerline ($x/L = 0$) are plotted for both the flow conditions analyzed. As it can be observed, the two solutions appear to be quite similar. In particular, in both cases, the wall jet effect seems to be absent and the velocity profiles appear to be almost linear for the most part of the cavity. Finally, in Fig. 19, the pressure coefficient $c_P$ is plotted versus the curvilinear abscissa computed along the solid wall, starting from the flat plate origin [i.e., from the point $(-2, 0)$]. The pressure coefficient definition used herein is
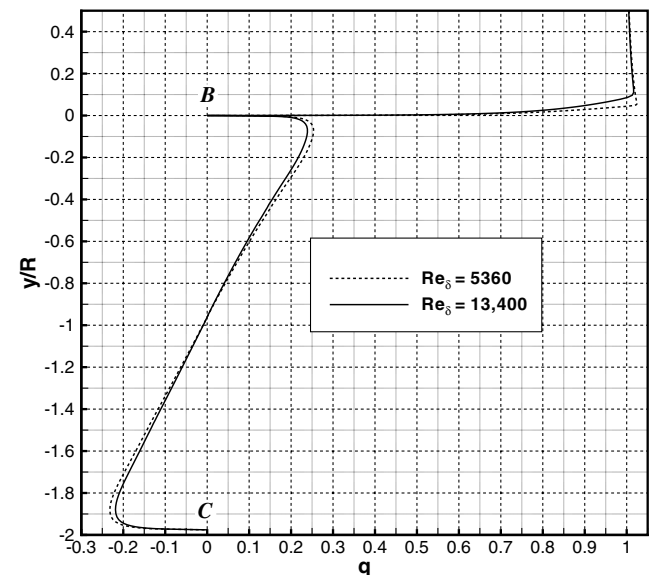


Fig. 18 Velocity profiles along the cavity centerline; $q(y) = u(0, y)/u(-1.0, 0.5)$. Case 1 (dashed line) and case 2 (solid line) of Table 1. Points B and C are relative to Fig. 17.
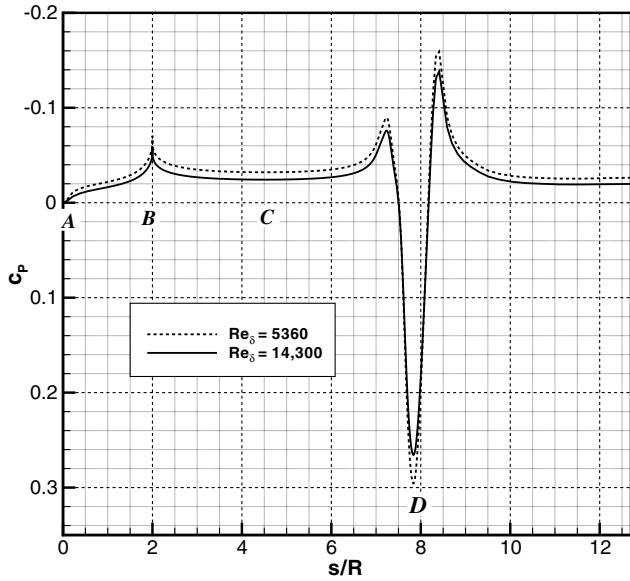
**Fig. 19 Pressure coefficient along the solid wall. Case 1 (dashed line) and case 2 (solid line) of Table 1. Points *A*, *B*, *C*, and *D* are relative to Fig. 16.**

$$c_p = \frac{p - p_{\text{ref}}}{\frac{1}{2}\rho_{\text{ref}} V_{\text{ref}}^2} \qquad (37)$$

where $p$ is the wall static pressure and $p_{\text{ref}}$ is the reference pressure, herein represented by the pressure value at the point $(-2, 0)$ of the computational domain shown in Fig. 15. In Eq. (37), $p_{\text{ref}}$ and $V_{\text{ref}}$ are the density and velocity magnitude outside the incoming boundary layer. The viscous pressure distribution along the solid wall is similar to what has been observed from the flow calculations based on inviscid methods, that is, the flow accelerates up to the cusp point, whereas the inviscid velocity along the cavity periphery is almost constant except in proximity of both the cusp point and the stagnation

point. The stagnation point in both cases occurs at $x/l \approx 0.75$. It is worth noting that, in this flow, the stagnation point is located downstream of both the incoming wall boundary layer and the next shear layer where viscous losses occur. This explains why the pressure coefficient at the stagnation point is not equal to one. Furthermore, by moving from the stagnation point toward the left, the flow accelerates within a very small distance and, next, it gradually decelerates to match the constant velocity region inside the cavity. Similarly, by moving from the stagnation point toward the right, the flow rapidly accelerates and next follows a smoother deceleration.

## VI. Approximating Reynolds-Averaged Navier–Stokes Solution with Batchelor-Model Flow

We now go back to the inviscid model (the Prandtl–Batchelor model) where we adjust the jump in the Bernoulli constant to fit the flow speed inside the cavity. In particular, we consider the vertical velocity profile passing through the cusp that we obtain from the RANS simulation at $Re_\delta = 5360$. The jump in the Bernoulli constant $\beta$ is adjusted by a trial-and-error method until the slope of the velocity inside the cavity obtained by the Prandtl–Batchelor model is as close as possible to the one obtained by the RANS model. The velocity contour plot corresponding to this case is shown in Fig. 20, and Fig. 21 shows the vertical velocity profile across the cusp for the RANS solution and the Prandtl–Batchelor model.

The velocity profile can be divided into two regions: the region from the top boundary to the mixing layer where a potential flow takes place, and the inviscid rotational flow inside the cavity. It can be observed that the agreement between the RANS solution and the Prandtl–Batchelor model is remarkable. Also, the jump in the Bernoulli constant, which we can estimate from the velocity profile across the cusp, is $\beta' = 0.511$ and it agrees well with the value $\beta = 0.518$ that we impose through the discretized equations. This difference is a measure of the discretization error. Outside the cavity, in correspondence with the mixing layer, there is a flow acceleration that is predicted by both models. However, for $y \approx 0$, the Prandtl–
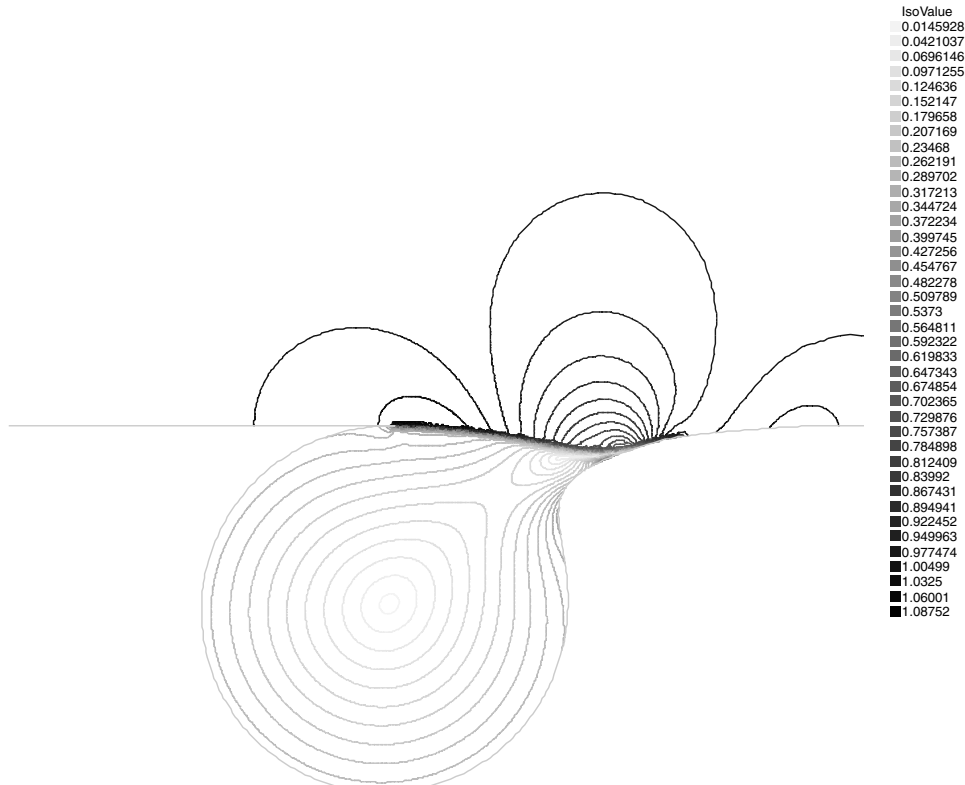


**Fig. 20 Velocity contour lines. The jump in the Bernoulli constant across the mixing layer was fitted to match the velocity profile obtained from the RANS simulation at $Re_\delta = 5360$.**
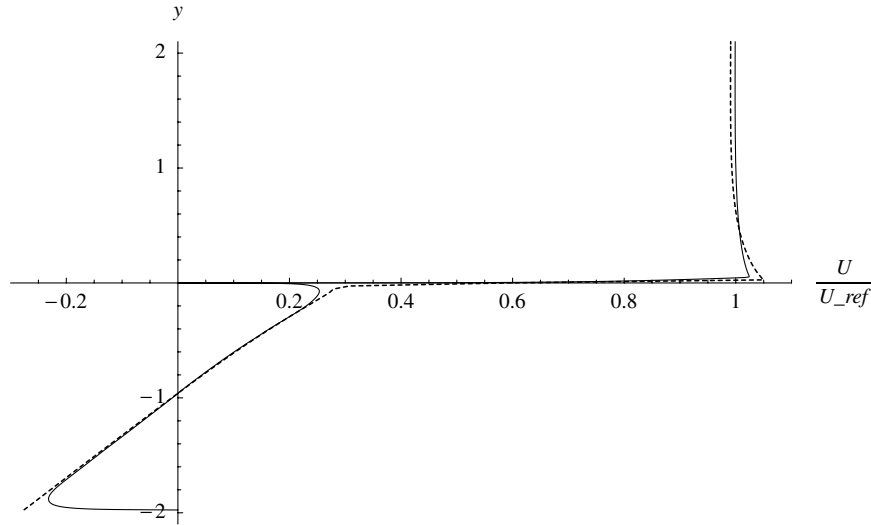
**Fig. 21  Comparison between the velocity profile obtained by the Prandtl–Batchelor model (dashed line) and the RANS at $Re_\delta = 5360$ (solid line); $x = 0$.**
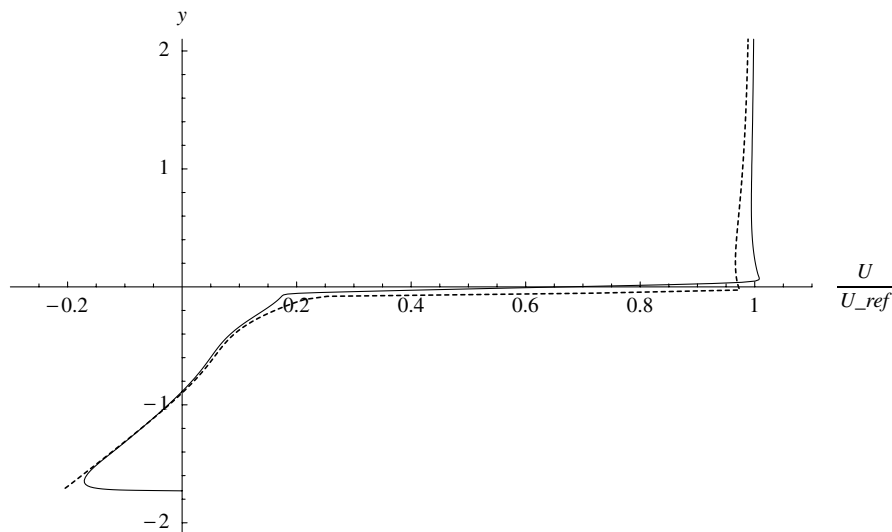


**Fig. 22  Comparison between the velocity profile obtained by the Prandtl–Batchelor model (dashed line) and the RANS at $Re_\delta = 5360$ (solid line); $x = 0.6$.**

Batchelor model predicts a larger velocity as compared with the RANS solution.

Of course, it is to be expected that because the mixing layer is reduced to a discontinuity curve in the Prandtl–Batchelor model, whereas it has a small but finite thickness in the RANS simulation, the two flowfields will be locally different. Also, in the RANS case, thanks to the development of a flat plate boundary layer on the lower wall between $x = -2$ and $x = 0$, there exists a displacement thickness that determines a slight overall acceleration of the flow, so that, for $y > 0.4$, the velocity predicted by the RANS model is slightly higher than the velocity at infinity. On the other hand, the velocity predicted by the Prandtl–Batchelor model for $y > 0.4$ is slightly less than one. This is due to the fact that the boundary condition imposed at the upper boundary is such that the line $y = 6$ is a streamline. The effect of this confinement is an overall reduction of the velocity as the bottom streamlines are diverging up to the rear stagnation point, as seen in Fig. 20. These differences in the velocity distribution will have an influence on the predicted pressure outside the cavity, as will be discussed next. Comparing the velocity profiles at different $x$ locations, Figs. 22 and 23, we see that the difference at the edge of the mixing layer becomes larger, whereas, inside the cavity, the comparison is still good.

For the Prandtl–Batchelor model, the value of the pressure inside the cavity is computed by taking

$$B(\psi) = \tfrac{1}{2} - \beta H(-\psi)(1 - \psi) \qquad (38)$$

and

$$p = B(\psi) - \tfrac{1}{2}(u^2 + v^2) \qquad (39)$$

In Figs. 24 and 25, we compare the pressure coefficient profiles across a vertical line through the point $x = 0$. The pressure taken as reference is the pressure at the upper boundary of the Prandtl–Batchelor simulation ($x = 0$, $y = 6$) for Fig. 24, whereas, for Fig. 25, the reference pressure is that at the center of the cavity ($x = 0$, $y = -1$).

Inside the cavity, the pressure coefficient profiles are almost perfectly superimposed (see Fig. 25). As expected, across the mixing layer, the variation of the pressure coefficient differs in the two cases because the local velocity fields are different. In particular, the velocity profiles show that the actual Bernoulli constant jump across the mixing layer differs in the two cases. In the Prandtl–Batchelor case, it is larger because the velocity above the mixing layer is larger, although the slopes of the velocity profiles are the same (see Fig. 21). The difference in the Bernoulli constant jump is equal to the difference in the pressure coefficient observed in Fig. 24 for $y = 0$. For $y > 1$, the predictions settle on two different values of the pressure coefficient. This is due to the fact that the velocity for
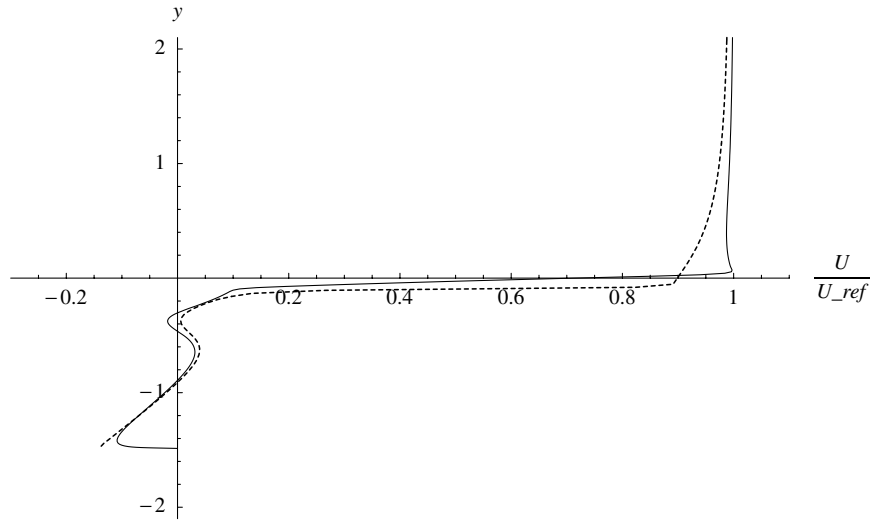
**Fig. 23   Comparison between the velocity profile obtained by the Prandtl–Batchelor model (dashed line) and the RANS at $Re_\delta = 5360$ (solid line); $x = 0.8$.**
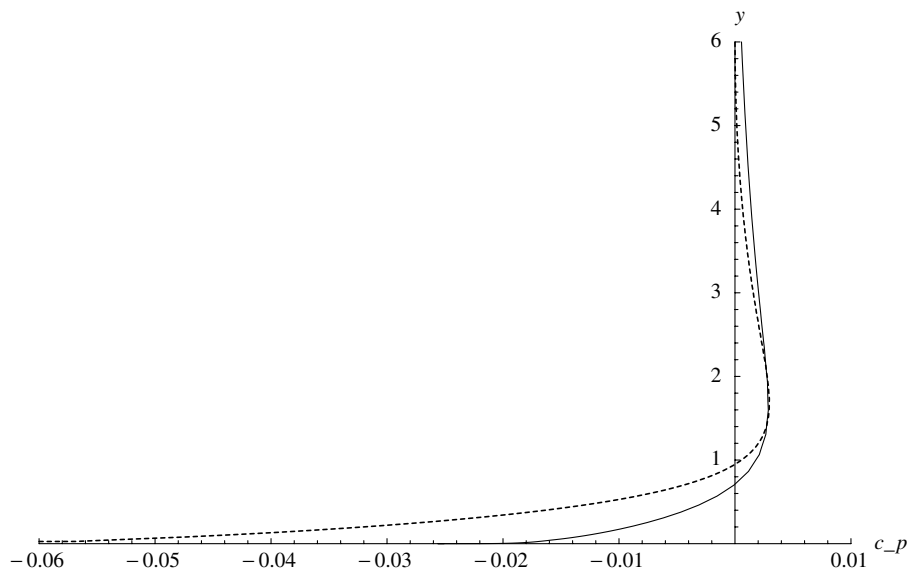
**Fig. 24   Comparison between the pressure coefficient outside the cavity obtained by the Prandtl–Batchelor model (dashed line) and the RANS at $Re_\delta = 5360$ (solid line); $x = 0$.**
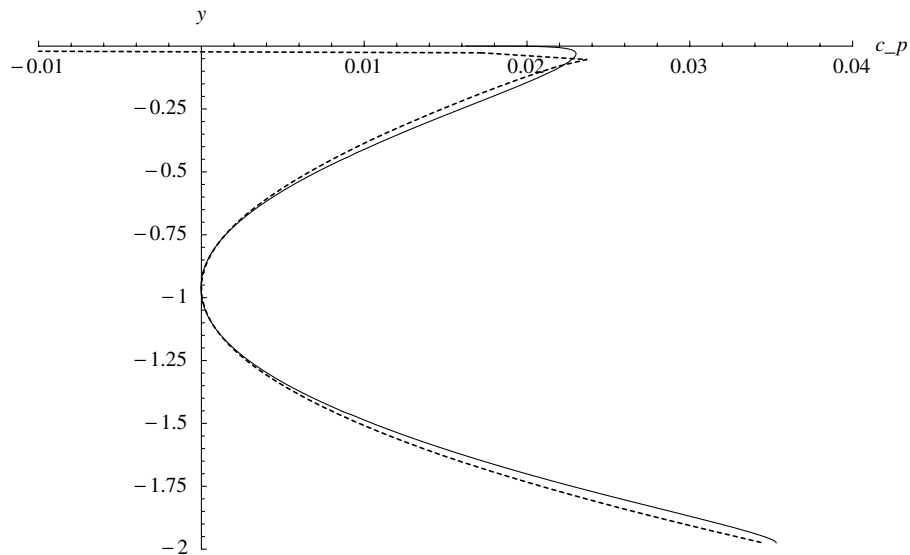
**Fig. 25   Comparison between the pressure coefficient inside the cavity obtained by the Prandtl–Batchelor model (dashed line) and the RANS at $Re_\delta = 5360$ (solid line); $x = 0$.**
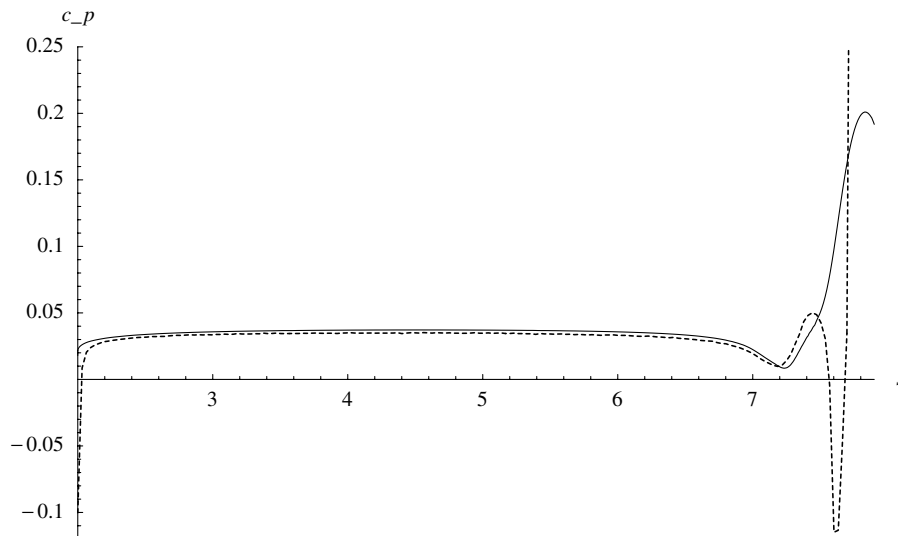
$c\_p$



**Fig. 26  Comparison between the pressure coefficient obtained by the Prandtl–Batchelor model (dashed line) and the RANS (solid line) along the cavity wall.**

$y > 0.4$ tends to a value that is slightly less than one for the Prandtl–Batchelor model and slightly more than one for the RANS model, as mentioned earlier. Inside the cavity for $y = 0$, both models predict a spike in the pressure due to the presence of the cusp at $x = y = 0$. In that region, however, formula (38) fails, as argued next.

The pressure coefficient along the cavity wall is presented in Fig. 26. The cusp is located at $s = 2$, and the rear stagnation point is at about $s = 7.7$, as predicted by both models. Within these two points, the flow rotates inside the cavity from larger values of $s$ to smaller values. We observe that the RANS and the Prandtl–Batchelor predictions almost coincide except close to the cusp and close to the rear stagnation point. In these regions, for the Prandtl–Batchelor model, we have $\psi \approx 0$ because the separatrix is defined by $\psi = 0$. Therefore, the regularization error introduced in the discretization of the Dirac function causes the discrepancy between the results of the two models. In other words, next to the separatrix or close to the rear stagnation point, there is no sharp jump in the Bernoulli constant but rather a region where the Bernoulli constant varies as a function of $\psi$, and therefore formula (38) is not accurate anymore.

Finally, we note that the cavity that we designed by a simple potential flow shows flow characteristics that are compatible in a first approximation, with a steady (probably unstable) trapped vortex. In other words, the choice of $cav_{50}$ geometry is such that the RANS solution shows a large zone of almost constant flow speed corresponding to a weak adverse pressure gradient without secondary separations.

## VII.  Conclusions

An overall appreciation of the preceding results leads us to the conclusion that a Prandtl–Batchelor model can represent a useful simplified model to study and design vortex trapping cavities. For the cases presented, the Prandtl–Batchelor model solution is obtained in about a minute, whereas the RANS solution takes a couple of hours on comparable computers. Therefore, the model that we described can be used as a fast and accurate surrogate of RANS simulations in an optimization loop to the end of designing a vortex trapping cavity. The main ingredient to get an appropriate representation of the flow is the determination of the correct jump in the Bernoulli constant. In this paper, the jump was fitted to data obtained from a RANS simulation. The RANS model was in turn validated by comparing it to experimental results. In general, the jump in the Bernoulli constant can be computed by imposing the compatibility of the cyclic layer with the inviscid solution, as done for a laminar case in [11,19]. Therefore, the main result of this work is to show that the Prandtl–Batchelor model with an appropriate jump of the Bernoulli constant gives an accurate approximation of both flow velocity and pressure

inside a vortex cavity. These results are a necessary prerequisite that now makes meaningful the coupling of the Prandtl–Batchelor model to an appropriate cyclic boundary-layer code to simulate the flow inside vortex cells. This model will provide an efficient tool for the optimization of vortex cavities, as compared to a RANS simulation. We plan to apply the model detailed in this paper to design vortex cavities that will actually be tested on bumps and airfoils. In this sense, ongoing wind-tunnel experiments on vortex cavities at Southampton University and Centro Italiano Ricerche Aerospaziali will provide additional data to calibrate the model we used for design.

## References

[1]  Kasper, W. A., "Aircraft Wing with Vortex Generation," U.S. Patent No. 3831885, 27 Aug. 1974.

[2]  Savitsky, A. I., Schukin, L. N., Karelin, V. G., Mass, A. M., Pushkin, R. M., Shibanov, A. P., Schukin, I. L., and Fischenki, S. V., "Method for Control of the Boundary Layer on the Aerodynamic Surface of an Aircraft, and the Aircraft Provided with the Boundary Layer Control System," U.S. Patent No. 5417391, 23 May 1995.

[3]  Kruppa, E. W., "A Wind Tunnel Investigation of the Kasper Vortex Concept," *AIAA 13th Annual Meeting and Technical Display Incorporating the Forum on the Future of Air Transportation*, AIAA Paper 1977-310, 1977.

[4]  Wu, J. M., and Wu, J. Z., "Vortex Lift at a Very High Angle of Attack with Massively Separated Unsteady Flow," *Fluid Dynamics of High Angle of Attack* edited by R. Kawamura and Y. Aihara, Springer, New York, 1993, pp. 35–63.

[5]  Ringleb, F. O., "Separation Control by Trapped Vortices," *Boundary Layer and Flow Control*, edited by G. V. Lachmann Vol. 1, Pergamon, London, 1961, pp. 265–294.

[6]  Routh, E. J., "Some Applications of Conjugate Functions," *Proceedings of the London Mathematical Society*, Vols. s1-12, No. 1, 1880, pp. 73–89.
doi:10.1112/plms/s1-12.1.73

[7]  Gurevich, M. I., "On an Error of F. O. Ringleb," *Izvestiya Akademii Nauk SSSR, Mekhanika Tverdogo Tela*, No. 1, 1965, pp. 205–206 (in Russian).

[8]  Rossow, V. J., "Aerodynamics of Airfoils with Vortex Trapped by Two Spanwise Fences," *Journal of Aircraft*, Vol. 31, No. 1, 1994, pp. 146–153.
doi:10.2514/3.46467

[9]  Ladyzhenskaya, O. A., *The Mathematical Theory of Viscous Incompressible Flow* Izdatel'stvo Fiziko-matematicheskoi Literatury,

Moscow, 1961 (in Russian) (English Translation published by Gordon and Breach, New York, 1969).

[10] Batchelor, G. K., "A Proposal Concerning Laminar Wakes Behind Bluff Bodies at Large Reynolds Number," *Journal of Fluid Mechanics* Vol. 1, No. 4, 1956, pp. 388–398.
doi:10.1017/S0022112056000238

[11] Bunyakin, A. V., Chernyshenko, S. I., and Stepanov, G. Yu., "High-Reynolds-Number Batchelor-Model Asymptotics of a Flow past an Airfoil with a Vortex Trapped in a Cavity," *Journal of Fluid Mechanics* Vol. 358, March 1998, pp. 283–297.
doi:10.1017/S0022112097008203

[12] Koenig, K., and Roshko, A., "An Experimental Study of Geometrical Effects on the Drag and Flow Field of Two Bluff Bodies Separated by a Gap," *Journal of Fluid Mechanics*, Vol. 156, July 1985, pp. 167–204.
doi:10.1017/S002211208500204X

[13] Baranov, P. A., Guvernyuk, S. V., Zubin, M. A., and Isaev, S. A., "Numerical and Physical Modeling of the Circulation in a Vortex Cell in the Wall of a Rectilinear Channel," *Fluid Dynamics*, Vol. 35, No. 5, Sept. 2000, pp. 663–673.
doi:10.1023/A:1026682629971

[14] Isaev, S. A., Guvernyuk, S. V., Zubin, M. A., and Prigorodov, Yu. S., "Numerical and Physical Modeling of a Low-Velocity Air Flow in a Channel with a Circular Vortex Cell," *Journal of Engineering Physics and Thermophysics*, Vol. 73, No. 2, 2000, pp. 337–344.
doi:10.1007/BF02681739

[15] Riddle, T. W., Wadcock, A. J., Tso, J., and Cummings, R. M., "An Experimental Analysis of Vortex Trapping Techniques," *Journal of Fluids Engineering*, Vol. 121, No. 3, 1999, pp. 555–559.
doi:10.1115/1.2823504

[16] Chernyshenko, S. I., "Stabilization of Trapped Vortices by Alternating Blowing-Suction," *Physics of Fluids*, Vol. 7, No. 4, 1995, pp. 802–807.
doi:10.1063/1.868603

[17] Cattafesta, L., Williams, D. R., Rowley, C. W., and Alvi, F., "Review of Active Control of Flow-Induced Cavity Resonance," AIAA Paper 2003-3567, 2003.

[18] Pastoor, M., Henning, L., Noack, B. R., King, R., and Tadmor, G., "Feedback Shear Layer Control for Bluff Body Drag Reduction," *Journal of Fluid Mechanics*, Vol. 608, Aug. 2008, pp. 161–196.

[19] Chernyshenko, S. I., "Asymptotic Theory of Global Separation," *Applied Mechanics Reviews*, Vol. 51, No. 9, 1998, pp. 523–536.

[20] Chernyshenko, S. I., Galletti, B., Iollo, A., and Zannetti, L., "Trapped Vortices and a Favourable Pressure Gradient," *Journal of Fluid Mechanics*, Vol. 482, May 2003, pp. 235–255.
doi:10.1017/S0022112003004026

[21] Zannetti, L., Chernyshenko, S. I., "Vortex Pair and Chaplygin Cusps," *European Journal of Mechanics, B: Fluids*, Vol. 24, No. 3, May–June 2005, pp. 328–337.
doi:10.1016/j.euromechflu.2004.09.005

[22] Savelsberg, R., and Castro, I. P., "Vortex Flow in Open Cylindrical Cavities," *Experiments in Fluids* [Online], Oct. 2008.
doi:10.1007/s00348-008-0575-4

[23] Batchelor, G. K., "On Steady Laminar Flow with Closed Streamlines at Large Reynolds Number," *Journal of Fluid Mechanics*, Vol. 1, No. 2, 1956, pp. 177–190.
doi:10.1017/S0022112056000123

[24] Lamb, H., *Hydrodynamics*, Cambridge Univ. Press, Cambridge, England, U.K., 1932.

[25] Zannetti, L., "Vortex Equilibrium in the Flow past Bluff Bodies," *Journal of Fluid Mechanics*. Vol. 562, Sept. 2006, pp. 151–171.
doi:10.1017/S0022112006001054

[26] Masotti, A., "Sulla Funzione Preliminare di Green per un'area Piana," *Atti del Seminario Matematico e Fisico di Milano*, Vol. 6, 1932, pp. 3–53.

[27] Chernyshenko, S. I., "Stratified Sadovski Flow in a Channel," *Journal of Fluid Mechanics*, Vol. 250, 1993, pp. 423–431.
doi:10.1017/S002211209300151X

[28] Donaldson, C. duP., "On the Form of the Turbulent Skin-Friction Law and its Extension to Compressible Flows," NACA, TN 2692, May 1952.

[29] Schlichting, H., *Boundary-Layer Theory*, McGraw–Hill, New York, 1979, p. 637.

[30] Wilcox, D. C., *Turbulence Modeling for CFD*, DCW Industries, La Canada, CA, 1993.

[31] Spalart, P., and Allmaras, S., "A One-Equation Turbulence Model for Aerodynamic Flows," AIAA Paper 92-0439, Jan. 1992.

[32] Menter, F. R., Kuntz, M., and Langtry, R., "Ten Years of Experience with the SST Turbulence Model," *Turbulence, Heat and Mass Transfer*, Vol. 4, edited by K. Hanjalic, Y. Nagano, and M. Tummers, Begell House, Redding, CT, 2003, pp. 625–632.

[33] Dacles-Mariani, J., Zilliac, G. G., Chow, J. S., and Bradshaw, P., "Numerical/Experimental Study of a Wingtip Vortex in the Near Field," *AIAA Journal*, Vol. 33, No. 9, 1995, pp. 1561–1568.
doi:10.2514/3.12826

[34] Vladimirov, V. A., and Tarasov, V. F., "Structure of Flow of a Viscous Liquid with Closed Streamlines," *Soviet Physics: Doklady*, Vol. 27, Jan. 1982, p. 17.

A. Plotkin
*Associate Editor*